Thesis Report

High Throughput Laser Communications to Tundra Orbits

AE5810: Thesis Space

Sander Orbons

Delft University of Technology | Airbus Netherlands

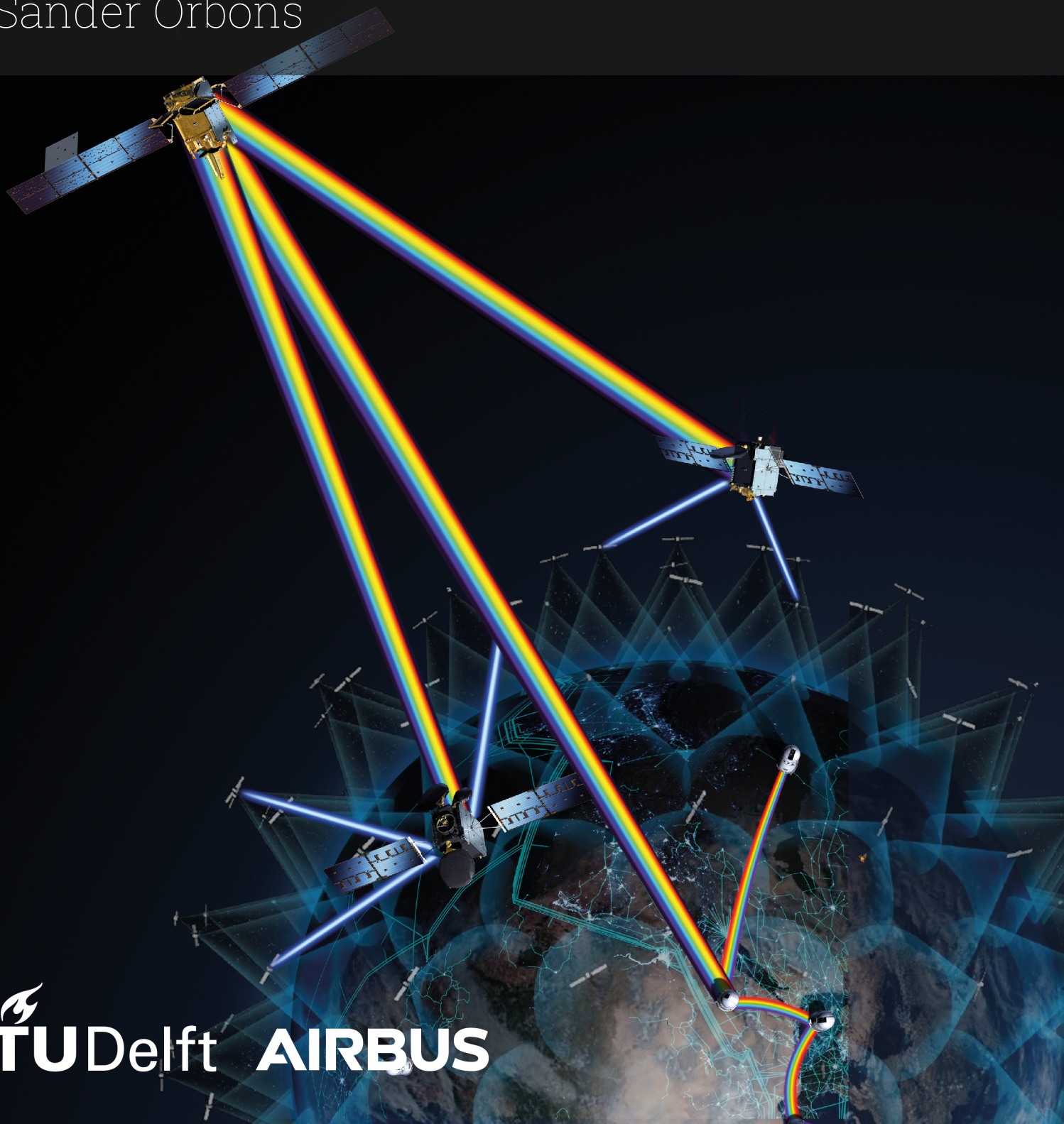

TU Delft AIRBUS

Thesis Report

High Throughput Laser Communications to Tundra Orbits

by

Sander Orbons

to obtain the degree of Master of Science
at the Delft University of Technology,
to be defended publicly on Tuesday May 28, 2024 at 01:00 PM.

Student number:	4668359	
Project duration:	May 16, 2023 – May 28, 2024	
Thesis committee:	Dr. Ir. R. Saathof,	TU Delft, supervisor
	Dr T. Dreischer,	Airbus Netherlands B.V., supervisor
	Dr. S.M. Cazaux,	TU Delft, chair
	Dr. J.A.M. Vanhamel,	TU Delft, examiner

This thesis is confidential and cannot be made public until December 31, 2024.

Style: TU Delft Report Style

An electronic version of this thesis is available at http://repository.tudelft.nl/.

TU Delft

Abstract

In an era which has been defined by the widespread adoption of digital connectivity, international data usage has seen exponential growth with global bandwidth more than doubling from 2020 to 2022 surpassing 1200 Tb/s. High throughput satellite connectivity has been growing accordingly from less than 2 Tb/s in 2018 to 27 Tb/s in 2023. With a new standard in satellites emerging: Very High-Throughput Satellites, which addresses a growing demand in throughput and bandwidth economics improvements by providing data rates in the order of terabit-per-second. Optical ground-to-satellite feeder links are a crucial technology to achieve throughput of such magnitude in ground-to-satellite communication.

Following the potential of optical feeder link applications and the improving maturity of laser communication technology, system architectures are being proposed to implement such feeder links. Most notably, very high throughput satellites in Geostationary orbit are considered to provide conventional broadband services or enable novel architectures such as 'fiber in the sky' with terabit-per-second throughput. However, optical links are highly susceptible to atmospheric losses due to turbulence, absorption, and scattering, especially at low link elevation angles. This presents a significant challenge for optical feeder link implementation in high-latitude areas, thus excluding large parts of Europe and North America from optical feeder link networks. Furthermore, previous system studies of very high-throughput satellites have yet to account for anisoplanatism on the effectiveness of ground-to-satellite pre-compensation in their link budget analysis. Addressing this issue is important due to the combined effects of large point-ahead angle and low link elevation angles to geosynchronous orbits.

This study explores an alternative architecture of two or three satellites in Tundra orbits to provide high elevation angle coverage to high-latitude regions, enabling the deployment of optical feeder links. The research examines various implementation aspects in Tundra orbits and performs a trade-off analysis to select an optimal orbit for servicing Canada, considering coverage, radiation environment, pointing angles, and delta-v requirements. Additionally, a link budget analysis evaluates optical feeder link performance, including dynamic turbulence penalties. The simulations focus on angular anisoplanatism and highlight the link geometry impact on adaptive optics efficacy. Our analysis shows a mean link budget improvement of 4.1 dB and 4.7 dB, resulting in uplink data rate improvements by factors of 2.56x and 2.94x for Tundra configurations with two and three satellites respectively. These findings suggest a cost-per-bit advantage for the two-satellite configuration and near break-even costs for the three-satellite array. Moreover requiring significantly smaller link margins for strong turbulence resistant operations. Overall, this study demonstrates the feasibility and potential of Tundra constellations to enhance high-throughput satellite communication, offering robust and efficient service in regions where GEO systems face limitations.

Contents

Nomenclature

Abbreviations

BER	Bit Error rate
BPSK	Binary Phase Shift Keying
CDF	Cumulative Distribution Function
CNES	Centre National d'Études Spatiales
ECEF	Earth-centered, Earth-fixed coordinate system
ECI	Earth-Centered Inertial reference frame
EOL	End-Of-Life
ESA	European Space Agency
FoV	Field of View
FSOC	Free-Space Optical Communication
GCR	Galactic Cosmic Rays
GEO	Geostationary Orbit
GNSS	Global Navigation Satellite System
GSO	Geosynchronous Orbit
HEO	High Eccentric/Elliptic Orbit
HTS	High-Throughput Satellite
ICSO	International Conference on Space Optics
LAN	Longitude of the Ascending Node
LEO	Low Earth Orbit
MEO	Middle Earth Orbit
NGSO	Non-Geosynchronous Orbit
OFL	Optical Feederlink
OGS	Optical Ground Station
OGS	Optical Groundstation
PAA	Point Ahead Angle
PDF	Probability Density Function
QZSS	Quasi-Zenith Satellite System
RAAN	Right Angle of the Ascending Node
RF	Radio frequency

Rx	Receiver
SEU	Single Event Upset
SNR	Signal to Noise Ratio
SPENVIS	Space Environment Information System
STK	Systems Toolkit
SWaP	Size, Weight and Power
TID	Total Ionisation Dose
Tx	Transmitter
VHTS	Very-High Throughput Satellite

Symbols

α_{paa}	Point ahead angle
γ	Attenuation coefficient
λ	Wavelength
ω	Argument of perigee
σ	Standard deviation
σ_I	Scintillation index
$\sigma_{\phi,\theta}$	Anisoplanatism phase variance
σ_ϕ	Phase variance
θ_0	Anisoplanatic angle
θ_{div}	Divergence angle
θ_{TA}	Isokinetic angle
ξ	Zenith angle
e	Eccentricity
i	Inclination
r_0	Fried parameter
w_0	Beamwaist
fig	Tip-tilt correction
D	Aperture diameter
k	Wavenumber
L	Propagation distance

1 Introduction

In an era marked by the widespread expansion of digital connectivity, international data usage has been witnessing exponential growth with global bandwidth more than doubling from 2020 to 2022 to surpass 1200 Tb/s [1]. High throughput satellite connectivity has been growing accordingly from just under 2 Tb/s in 2018 to over 27 Tb/s in 2023 [2], providing consumer broadband, cellular backhaul, trunking, and other connectivity services.

Given the uneven spread of population and economic activity over the globe, regional coverage through Geostationary orbits remains a crucial vector to effectively meet this demand [3]. Satellite service providers have been innovating to accommodate the growing demand and improve bandwidth economics. The anticipated system throughput for a single regional High-Throughput Satellite (HTS) in Geostationary orbit is expected to grow from 0.75 Tb/s to 3.75 Tb/s by 2028, with costs projected to decrease to 1€/Gb [3]. Operational HTS have already grown accordingly from 90 Gb/s in 2010 to 1 Tb/s in 2023 with the Viasat-3 satellites. Introducing a new category which very well could become a standard: Very High-Throughput Satellite (VHTS), able to provide terabit-per-second throughput [4].

The ability to deliver terabit-per-second data rates to very high-throughput satellites is significantly constrained by the ground-to-space feeder link. RF-based feeder links, operating in the Ka-band, Q/V-band, and W-band, offer only 5 to 10 GHz bandwidth per gateway. Necessitating at least 20 active ground stations to achieve very high-throughput to a single satellite [5]. Furthermore, large swaths of these frequencies are not available for commercial usage and the spectrum which is available is highly sought after. Leading to unsustainable rise of ground infrastructure costs for satellite further capacity growth. Optical Feeder Links (OFL) are a promising technological solution capable of enabling terabits-per-second (Tb/s) throughput from ground-to-space. Utilizing the near-infrared spectrum with several terahertz (THz) of license-free bandwidth per ground-station, moreover freeing up the valuable RF spectrum to be fully dedicated to user links. The highly directive nature of optical beams, which rapidly decorrelate in the atmosphere, enhances data privacy and enables the placement of optical ground stations and satellites in close proximity. Additionally, transceiver hardware requires lower size, weight, and power (SWaP) on satellites. Optical communication links have considerable space flight heritage, most notably in space-to-space applications such as those with the European Data Relay System (EDRS) since 2016 [6]. Optical feeder links however have lower technological maturity, with significant ongoing development efforts focused on enhancing adaptive optics pre-correction for uplinks.
Despite these advantages and developments, the reliable propagation of optical waves through the atmosphere poses considerable challenges. In order to ensure cloud-free line-of-sight visibility of 99.5% and higher, site diversity mitigation strategies involving 5-14 Optical Ground Stations (OGS) are necessary. Furthermore, variations in attenuation, absorption, and turbulence can impact signal quality, potentially leading to optical feeder link outages and complicating the achievement of the 99.9% availability required for VHTS by service providers [4]. Despite these challenges the potential of OFL development is widely recognised and system studies have been proposing OFL implementations for VTHS. Notably considering implementations through Geostationary Orbit (GEO) architectures. This commonly proposed orbit however, is ill-suited to service high-latitude regions as it does not allow for sufficient elevation angles when establishing a link through the atmosphere from 50+ deg latitudes. Excluding the placement of OGS at large economic hubs in Europe and North-America. Additionally, the effectiveness of optical feeder links to GEO is further compromised by anisoplanatism, particularly due to the large point-ahead angle and low link elevation angles associated with this orbit. Anisoplanatism has

significant implications on the system's ability to perform effective ground-to-satellite pre-compensation, a crucial factor that has not been quantified in previous system studies.

An alternative architecture with two to three pseudo-geosynchronous satellites in Tundra Orbits, tailored for a long dwell time over Europe or Northern America, could provide continuous coverage with increased elevation angles at these high latitudes. The higher link elevation of 50+ deg over Canada or Northern Europe will enable the deployment of Optical Ground Stations at high latitudes and could yield a considerable link budget improvement by reducing atmospheric attenuation and turbulence. This could improve the link budget and increase the data rate and availability outlook for OFL. The inclusion of more high-latitude OGS could further open the way for new applications like large-volume point-to-point optical data transfer for Governmental users and data centres.

The following thesis aims to determine the potential of a small Tundra constellation to serve as alternative to GEO for optical feeder link networks located in Canada. Establishing the implementation feasibility of Tundra orbits, selection of a suitable orbit and corresponding optical feeder link performance. To further introduce the research topic firstly chapter 2 will summarise the research gap and questions. Subsequently the research central to this thesis is presented in the form of a conference paper in chapter 3, concluded by a description of research conclusions and recommendation in chapter 4. Due to page limitations in the paper format additional information on select methodologies is provided in Appendix A-D.

2
Research objective

The following section arises from a literature study on optical feeder links and highly eccentric orbits, of which Tundra orbits are a subset.

2.1. Research Significance

The research conducted emerges from a notable absence of system level studies addressing the performance of OFL to Tundra orbits. Current research on OFL has been exclusively performed with very high-throughput satellites positioned in Geostationary orbit, following flight heritage of current high-throughput satellites. However, a review of literature suggests that there are definite advantages to the Tundra architecture for VHTS:

- Two satellite Tundra constellations can provide continuous link elevation angles of 50+ deg over high latitude coverage areas such as Northern-Europe [7] and North-America [8].
- Increased optical link elevation angle could lead to a considerable decrease in atmospheric attenuation [9] and turbulence penalties for OFL [10]. Potentially improving link margin and link availability under challenging atmospheric conditions.
- Anisoplanatism effects, while demonstrated to significantly affect adaptive optics efficacy [11], have been notably absent in GEO system study link budgets.
- The reduced isoplanatic-angle at high elevation angles [12], coupled with the low velocity of a satellite at the Tundra apogee could reduce anisoplanatism effects.
- The possibility to design a Tundra orbit for a long dwell time over Canada could allow a two or three satellite system to provide continuous coverage over the region, enabling the deployment of a domestic OGS network in Canada.

These advantages merit a study of the actual link budget performance for this new architecture. This includies the analysis of other factors impacting the feasibility of this concept:

- Radiation environment concerns due to perigee passes through the van Allen belts [13], restricting feasible orbits and orbit insertion strategy.
- Orbit maintenance ΔV cost restriction on the design of orbits at non-frozen inclination, imposing limits on coverage elevation angle maximisation.
- Orbit insertion ΔV cost must be considered to provide an orbit which has realistic launcher requirements.
- Sun exclusion properties during payload operations.

This study thus aims to design a system architecture and verify its performance as solution to the technical problems facing very high-throughput optical feeder links. This objective has been formulated as follows:

> Analysis of ground-space high throughput terabit-per-second optical feeder links to Tundra as a solution to reduce atmospheric attenuation and serve new high-latitude regions in Canada. By selecting suitable Tundra and evaluating feasibility and link performance, with specific focus on anisoplanatism and availability to Canadian optical ground stations relative to current GEO concepts.

2.2. Research Question

In the following section the research objective will be further defined in research questions, with a discussion on the set bounds on the scope. Following the observed, research gap the research question has been formulated as:

> To what extent could a Very High-Throughput Satellite constellation in Tundra improve space-ground optical feeder link throughput and availability in Canada when compared to the GEO architecture?

With the following sub-questions:

1. How does the ground-to-Tundra link architecture affect the optical link budget in an OGS feeder link network?
2. What is the optimal constellation and set of orbital parameters in Tundra Orbit for a continuous feeder link connection to an OGS network in Canada?
3. How does the Tundra architecture affect availability statistics for a Canadian OGS network?
4. To what extent is the implementation of Tundra feeder links competitive to proposed GEO designs?

Being a system level study the scope and level of detail has been limited to achieve results within the thesis framework.

Telecommunication is a broad topic with many possible architectures and even more use cases. In this study the scope has been considerably limited, by performing analysis of exclusively the feeder link element for Very-High Throughput Satellites in GEO and Tundra. Consequently the user links are not under consideration and the relevant use cases are not be analysed end-to-end but instead used as inputs for Quality of Service requirements for the feeder link.

With the study defined as a comparable analysis between a two and three Tundra constellation and one GEO satellites, Non-Geo-Synchronous Orbits (NGSO) are not considered. NGSO at Middle and Low Earth Orbit (e.g. O3B and Iridium, respectively) also provide an options for the coverage of specific regions however, in a much less efficient manner. That is to say requiring more satellites (10+ MEO and 20+ LEO [14]) with a lower duty cycle, and at lower elevation angles [15]. While constellations in these orbits could thus provide continuous regional coverage as well, this study does not consider these options as these occupy a different category from GEO with lower throughput and are generally implemented for global coverage solutions.

The analysis of ground to space communication in sub-question one does not aim to expand current methods but will instead focus on customary link modelling methods in order to provide an analysis which is readily compared to existing literature on OFL to VHTS.

Tundra orbits have been extensively studied in the past [16]. This research is focused on analysing the performance of these orbits for feeder links. As such, the extensive optimisation of the orbit for sub-question two is considered out of scope and will be limited to inputs addressing feasibility and orbit selections for coverage maximisation. Nonetheless considering a range of factors such as radiation impact, orbit maintenance, insertion and end-of-life solutions.

Sub-question three considers the impact of Tundra on the link availability under the influence of turbulence, limited to a single site. An extensive analysis of an OGS network with an availability analysis and optimisation such as performed by Poulenard [17] is considered out of scope.

3
Scientific article

The research performed in this thesis is presented as a conference paper following the intention to contribute a conference paper and presentation to the 2024 International Conference on Space Optics organised by CNES and ESA. An abstract has been entered and is awaiting acceptance.

Following ICSO guidelines this paper is limited to 20 pages. Consequently, additional material is provided in Appendices A-D to provide more background on implemented methodologies not addressed in the paper.

High Throughput Laser Communications to Tundra Orbits

Sander Orbons
Aerospace Engineering
Delft University of Technology
Delft, The Netherlands

***Abstract*—Future Very High-Throughput Satellites are foreseen to implement optical ground-to-satellite feeder links to achieve multi-terabit-per-second data rates. Optical links however, are highly susceptible to atmospheric losses caused by turbulence, absorption, and scattering, especially at low elevation angles. Despite prior confirmation of the feasibility of cloud-free network availability, high-latitude stations have been notably absent from optical feeder link studies due to the limitation of Geostationary orbits in providing sufficiently high link elevation angles. Tundra orbits present a promising alternative to Geostationary orbit, requiring two satellites to ensure uninterrupted coverage of high-latitude regions like Europe and Canada with link geometries highly suitable for optical communication. This paper addresses optical feeder link implementation aspects in Tundra orbits and selects a suitable orbit to service Canada while considering aspects such as coverage, radiation environment, pointing angles, and delta-v impact. End-to-end simulations, including downlink and uplink amplitude statistics, are presented to assess dynamic turbulence penalties. These simulations focus on angular anisoplanatism and highlight the link geometry impact on adaptive optics efficacy. This analysis anticipates a mean 4.1 and 4.7 dBm link budget advantage for Tundra configurations for two and three satellites respectively. These findings highlight Tundra constellations' potential to enhance satellite communication infrastructure, providing robust, efficient service in regions where Geostationary orbits faces limitations.**

***Index Terms*—Very High-Throughput Satellites, Optical Feeder Links, Tundra Orbits, Geostationary Orbits, Anisoplanatism**

I. Introduction

Continuing demand for capacity growth and cost reduction in satellite communication drive the development of Very High-Throughput Satellites (VHTS) with terabit-per-second (Tb/s) data rates. Optical Feeder Links (OFL) are considered a crucial technological development to effectively achieve up- and downlink of data rates of this magnitude. Free-space optical links namely provide license free-spectrum with data rates in the order of terahertz per ground station [1]. Freeing coveted RF-frequency spectrum for exclusive use on user-links and driving down ground segment cost for high throughput links [2]. Furthermore, the highly directive optical beams lower SWaP requirements and increase the difficulty for third parties to intercept the communication beam [1]. Site diversity is considered to ensure cloud-free line-of-sight visibility with 5-14 Optical Ground Stations (OGS) expected to achieve of 99.5+% availability [3]. Despite the potential of OFL, reliable propagation of optical waves through the atmosphere remains a challenge, with varying attenuation, absorption and turbulence impacting signal quality and potentially leading to OFL outages. Complicating site-diversity efforts to meet 99.9% link availability as required for VHTS applications [4]. Following the potential of OFL applications and the maturation of technology, systems are being proposed to implement OFL. Namely, VHTS in GEO as a platform providing broadband services or acting as a node in 'fibre in the sky' architectures [5].

The assumption in current research is that VHTS are, per definition, placed in GEO. Consequently, this architecture has also been studied to cover high-latitude regions such as Europe [6, 7, 8]. This orbit, however, is ill-suited to service high-latitude regions as it does not allow for sufficient elevation angles when establishing a link through the atmosphere from 50+ deg latitudes, excluding the placement of OGS at large economic hubs in Europe and Canada. Furthermore, previous system studies on OFL to GEO have yet to provide an estimation of the effect of anisoplanatism on the effectiveness of ground-to-satellite pre-compensation. This is especially concerning considering the compounded effect of large point-ahead angle and low link elevation to GEO.

An alternative architecture with two to three pseudo-geosynchronous satellites in Tundra orbits, tailored for a long dwell time over Europe or Northern America, could provide continuous coverage with increased elevation angles at these high latitudes. The high link elevation of 50+ deg over Canada or Northern Europe will enable the deployment of optical ground stations at high latitudes and could yield a considerable link budget improvement by reducing atmospheric attenuation and turbulence. Potentially improving the link budget, and increase the throughput and availability for OFL. The inclusion of more high-latitude OGS could furthermore open the way for new applications such as large-volume point-to-point optical data transfer for governmental users and data centres.

In this paper, the link budget performance of OFL from Canada to VHTS in Tundra orbits will be evaluated and compared to the conventional GEO architecture. Firstly, addressing link degradation under atmospheric turbulence, specifically focusing on anisoplanatism effects on adaptive optics tip/tilt pre-compensation. Followed by an overview of the general

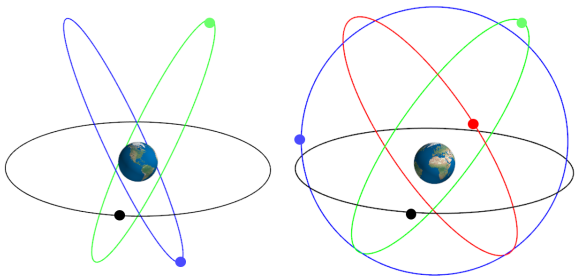

Fig. 1: Two and three Tundra constellation and Geostationary (black) orbit (Earth not to scale)

characteristics of Tundra orbits, addressing the feasibility and competitiveness of such orbits in contrast to GEO. To illustrate the potential of Tundra orbits, a case study is presented for an OGS network in Canada. Including an orbit selection which considers aspects such as pointing, radiation environment ΔV costs and optical link performance over the coverage region. Finally, link budget and availability improvements to be gained by moving from a single GEO to a two or three satellite Tundra constellation will be presented.

II. Optical feeder link description

This paper will focus on the link budget effect of moving the VHTS from GEO to Tundra and the impact on the high-throughput optical feeder link performance. Consequently, the performance of the user link is left outside the analysis. To place the OFL performance in the context of a generalized interpretation of the Quality of Service (QOS) requirements and performance metrics, the following three VHTS implementations serve as background:

- Broadband/broadcast service: Providing internet or telecom connection to regions and vehicles not covered by terrestrial infrastructure. QOS req. of 99.9% availability, performance metric is the minimization of cost/bit through maximisation of continuous throughput and reduction of ground-segment [4].
- Fibre in the sky entry point: Provide ground-space data transmission as entry and exit point for space based optical networks [9]. With similar QOS and performance as broadband services.
- High-volume point-to-point transmission: Optical transmission of very large data volumes of opportunity through a bent-pipe architecture, relevant for secure data transmission for governmental and data center users at high-latitudes. Does not require continuous OFL availability and performance is measured in maximisation of accumulated data throughput.

In defining the architecture, GEO is considered as baseline for the two and three satellite constellations in Tundra orbits. Each satellite employing multiple laser communication terminals to achieve a total 1 Tb/s throughput [10]. With a segmentation of the ground based apertures over two or more pointing assemblies to provide a step-wise satellite hand-over for the Tundra constellation. Furthermore employing a network of OGS to offer near-continuous OFL availability spread over the coverage area of interest.

In the configuration of the optical link under analysis, the signal wavelength is considered to be 1550 nm following SDA and CCSDS standards. Further benefiting from a wide atmospheric transmission window [11], commercial hardware availability and eye safety considerations [12, Chapter 1]. Next, owing to the analysis of high data rate links, receiver detection is performed using a homodyne coherent detector. Suitable for very high data rates with high powers, requiring more complex hardware and phase matching but yielding better BER performance [12, Chapter 4]. Continuing on detection methods, binary phase shift keying (BPSK) is chosen as the modulation format and no coding will be considered. Such a receiver architecture has already successfully been applied to 5.6 Gb/s ground-satellite links (1064 nm) [13].

A. Link performance drivers

The performance of a single uplink and downlink beam is evaluated through a link budget analysis. In optical uplinks and downlinks, three geometrical parameters can be recognised as drivers of the link budget and differentiating between a GEO and a Tundra satellite. Recognising their influence on the performance of an optical link is crucial in comparing different system architectures and performing a later trade-off.

1) Slant path: The link elevation angle is responsible for lengthening the propagation path through the atmosphere. Geometrically, accounting for the curvature of the Earth, this is [14]:

$$L(\xi)=\sqrt{(R_E+h_0)^2+2z\ cos(\xi)\cdot(R_E+h_0)+z^2} \\ -R_e-h_0, \tag{1}$$

with ξ the zenith angle, z the propagation distance and L the lengthened propagation path through the atmosphere. An expression often approximates by $sec(\xi)$. Following Equation 1, the atmospheric propagation path through a 20km thick atmosphere at a 30 deg elevation would be lengthened by a factor 2, increasing the effects of atmospheric attenuation and turbulence.

2) Spreading: Spreading represents the fundamental loss of signal power as it geometrically spreads through free-space, characterised by:

$$L_{FSL}=\left(\frac{\lambda}{4\pi\cdot L}\right)^2 \tag{2}$$

by convention this is expressed in free-space loss, requiring a multiplication with the signal wavelength.

3) Point ahead angle: Due to the satellite velocity and limited speed of light there is an offset-angle between the uplink and downlink path. This point ahead angle is a function of the satellite orbit and provides challenges in the adaptive optics compensation

$$\alpha_{paa}=2\frac{v_t}{c}, \tag{3}$$

where v_t is the tangential velocity of the satellite and c the speed of light.

These three parameters present the fundamental difference in link geometries influencing link budget performance. Following these effects, the modelling approach of atmospheric effects and anisoplanatism will be discussed in detail, respectively influenced by slant path and point ahead angle.

III. Atmospheric losses modelling

Atmospheric attenuation and turbulence present a significant challenge for optical feeder links. The modelling of these effects will will be highlighted here.

Random and dynamic variations in the refractive index of the atmosphere due to temperature fluctuations in mixing air masses impact the propagation of light beams. The optical signals propagating through these turbulent layers experience phase shifts, intensity fluctuations, and beam wandering, degrading the quality and reliability of the communication link. Accurate modelling of atmospheric turbulence conditions and effects is therefore crucial. The methodology presented here is based on analytical models developed from the Rytov approximated wave equation solution with a varying refractive index.

A. Static attenuation

Atmospheric channel attenuation primarily stems from absorption and scattering, notably significant at low-elevation angles. The LOWTRAN 7 model [15] was used to determine representative atmospheric transmittance under different atmospheric conditions. Matlab and Python code wrappers have been employed to use this native Fortran code to determine aerosol [16] and molecular [17] attenuation. From this model, two sky conditions given in Table I were determined. Scaling with zenith angle as Equation 1.

TABLE I: Lowtran inputs

	Benign scenario	Challenging scenario
Climate	Mid-latitude summer	Mid-latitude summer
Aerosols	Rural	Urban
Total attenuation	-0.45 dB $\xi = 0°$	-2.10 dB $\xi = 0°$

B. Turbulence conditions

The turbulent condition of the atmosphere is represented here using the refractive index structure constant $C_n^2(h)$, indicating the variation of the refractive index due to small fluctuations in temperature along the propagation path. While the exact vertical profile largely depends on local conditions, the Hufnagel-Valley is generally accepted for sizing studies as a baseline profile for mid-latitudes. Here adapted for a profile h_0 meter above sea-level by Giggenbach [18]:

$$C_n^2(h) = 0.00594(\frac{v}{27})^2(10^{-5}h)^{10}e^{-h/1000} + 2.7 \cdot 10^{-16}e^{-h/1500} + A \cdot e^{(h-h_0)/100}, \quad (4)$$

where v and A are the rms wind-speed (m/s) and C_n^2 at ground-level, respectively. To summarise the turbulence conditions two parameters are presented which are integrated over the atmospheric propagation path. Firstly the Fried parameter, or atmospheric coherence width, [19]:

$$r_0 = \left[0.423k_0^2 \cdot sec(\xi)^{3/5} \int_0^L C_n^2(h)dh\right]^{-3/5}, \quad (5)$$

where k and ξ are the wave number and zenith angle, respectively. Describing the transverse width over which the atmospheric turbulence is correlated, a good indicator of boundary layer turbulence. The effect of coherence width is dependent on the link beam waist, consequently w_0/r_0 will be mostly used to generalise this parameter. The second parameter, the isoplanatic angle:

$$\theta_0 = \left[2.05k_0^2 \cdot sec(\xi)^{8/3} \int_0^L C_n^2(h)h^{5/3}\, dh\right]^{-3/5}, \quad (6)$$

defines the angular difference over which the turbulence over two path can be considered correlated [20]. The isoplanatic angle is strongly influenced by high-altitude turbulence, where high altitude winds such as the jet stream severely reduce θ_0.

Generally the Hufnagel-Valley 57 turbulence profile, representing $r_0 = 19cm$ and $\theta_0 = 24\mu rad$ at $\lambda = 1550nm$, is employed to indicate mean conditions. With the design of an OGS network driven by cloud-free line-of-sight probability to achieve a consistent availability of 99.9+%, it is imperative to prevent the need for additional site-diversity for turbulence mitigation. Coupled analysis of cloud probability and turbulence in Japan has shown that small-to-no turbulence link margins can reduce the availability of an OGS network with up to 10 percent points [21]. Consequently to prevent the need for additional site-diversity a robust link-margin for long-term and short-term variability in turbulence conditions is necessary.

To estimate the long-term turbulence conditions, the expansive r_0 and θ_0 nighttime measurements by Walters [22] provide general statistics of cloud-free turbulence conditions across the United States. A limitation of this dataset is the lack of daytime measurements, whereas around-the-clock OFL operations are considered. However, we can reliably use the nighttime θ_0 statistics for daytime conditions, mainly influenced by high-altitude turbulence without strong diurnal or site-dependent variations. Measurements of r_0, however, are significantly influenced by boundary layer conditions with pronounced diurnal and site-dependent variations. Long-term measurements at White Sands indicate that the standard deviation factor of r_0 between daytime and nighttime remains relatively stable [23] with a consistent reduction of factor 2.16 in mean r_0 during daytime. Data from Allis et al. corroborate this trend of diurnal variation in r_0 [24]. From this observation, the r_0 log-normal distribution in [22] is extend to encompass a projected day and night r_0 distribution. This is given in Figure 2.

In addition to long-term variability, a point of concern for continuous operations is the short-term stability of atmospheric conditions. With the majority of turbulence measurements

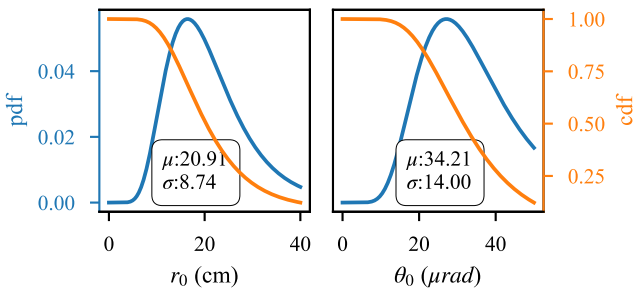

Fig. 2: r_0 and θ_0 at Zenith distribution for $\lambda = 1550nm$

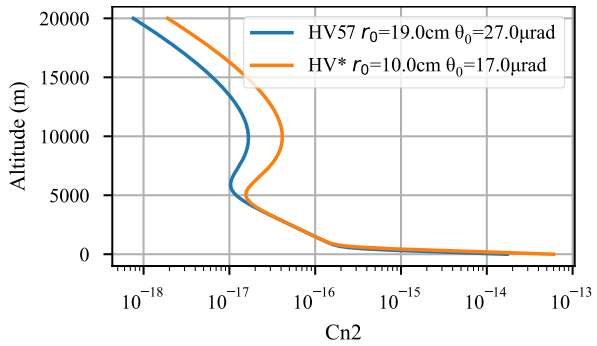

Fig. 3: Hufnagel-Valley Cn_2 profile at zenith

done for long-term averages relevant to astronomical observation, short-term degradation of optical communication link conditions is a concern acceptable. The temporal stability of 4 locations is considered by Ramio et al. [25]. Showcasing that while a mean θ_0 is achieved of 26-41 μrad (at $1550nm$), θ_0 remains 26 μrad for 30 consecutive minutes (mean) at most. This is further supported by isoplanatic angle measurements at the TU Delft rooftop and previously documented by Eaton et al. [26].

Considering the variability of atmospheric turbulence conditions described, and the need for continuous operations given a cloud-free line-of-sight, stronger turbulence conditions are to be included in link budgets for system proposals. In addition to the general HV57, a Hufnagel-Valley profile has been scaled to represent a 99% probability condition and given in Figure 3 with ground-level turbulence and rms wind velocity of $A = 5.985e-14$ and $v = 33.3m/s$.

C. Mitigation techniques

To enhance the reliability of a link in turbulent conditions, a variety of mitigation techniques can be employed. This study includes the commonly considered techniques of aperture averaging and adaptive optics pre-compensation.

By increasing the receiving aperture diameter, small signal variations which ordinarily lead to scintillation can be averaged out. This method is exclusively considered for downlinks as sizing of space terminals to accommodate receiving aperture diameters sufficiently large is not favourable with a noticeable aperture averaging factor for $D_R/r_0 > 1$.

Adaptive optics uplink pre-compensation involves adjusting the wavefront of the outgoing beam at the transmitter with the conjugate of the wavefront distortions measured at the receiver, effectively pre-correcting for atmospheric turbulence along the corresponding propagation path. In this study, the evaluation is limited to tip-tilt corrections, which, for weak turbulence conditions, corresponds to the elimination of 86 % of the phase errors [27].

In strong atmospheric boundary conditions, full adaptive optics compensation is much more effective [28], visible in the results of the recent uplink demonstration to Alphasat [29]. Here, an improvement of 10dB is visible for a full AO correction over tip-tilt only, for $r_0 < 5cm$ at $P < 10^{-1}$. However, little perceivable difference in the uplink irradiance under weak boundary layer turbulence ($r_0 = 6 - 14cm$) is visible. The consistency of the losses under these conditions is remarkable and could be attributed to high-altitude turbulence remaining uncorrected. This could be caused by the point ahead angle of the link to GEO leading to decorrelation of the uplink and downlink path at high altitude, referred to as anisoplanatism. Strong high-altitude turbulence can decorrelate the two wavefronts to such an extent that AO pre-correction would have an adverse effect. Full AO correction will degrade quicker under the influence of anisoplanatism [30]. For continuous operations with a large α_{paa}, only tip-tilt correction is considered, being more robust to high altitude turbulence.

This vulnerability to high altitude turbulence gives the relationship α_{paa}/θ_0 to characterise AO effectiveness. With θ_0 giving the angle over which the wavefront can be considered correlated, isolating just the tip-tilt component of the disturbance, the isoplanatic angle can be extended and defined as [31],

$$\theta_{TA} = \frac{0.184\lambda D^{1/6}}{\left[sec(\xi)^3 \int C_n^2(h) h^2 dh\right]^{1/2}} \tag{7}$$

For the two profiles, HV57 and HV* this gives $\theta_{TA}/\theta_0 = 1.86, 2.00$ for $D = 20cm$ respectively. Giving an isokinetic angle significantly large enough for continuous operations with $\alpha_{paa} = 18.5\mu rad$ in GEO and Tundra uplinks.

D. Signal scintillation

Signal power will occasionally fade at the receiver due to beam-wander and signal interference induced by propagation through atmospheric turbulence. To estimate these effects on a finite beam for both uplink and downlink paths, analytical and semi-empirical methods adapted from the general Rytov approximation have been implemented. Providing a scintillation margin for which, with probability p, it can be said that the signal power would not fade beyond that margin.

The uplink model, based on Parenti [32], separates near-field and far-field effects into distinct probability density functions (PDFs) for the scintillation index. Here respectively as a Log-normal and Weibull distribution. This method accounts for scintillation caused by beam-wander in a tip-tilt corrected system employing beam-tracking. This method has been validated

for vertical and horizontal propagation, ensuring confidence in its application to slant path propagation, with results closely corresponding to those reported by Andrews [33].

Downlink scintillation is modelled analytically and adapted for slant paths with strong turbulence. Furthermore accounting for an aperture averaging effect at the ground receiver via the methodology by Andrews [34].

E. Signal Strehl

Turbulence will further impact the quality of the focused wavefront in the fibre due to signal phase variations at the receiving aperture plane. Generally, the mean fibre coupling losses are accounted for using a Strehl ratio, such as for tip-tilt corrected beams from [27],

$$[S]_{fig} = 0.134(D/r_0)^{5/3} \tag{8}$$

A widely used and simple expression of which new analytical or empirical improvements have been developed to be valid in more scenarios [35][36]. A limitation in this expression is that it fails to account for anisoplanatic effects impacting the effectiveness of adaptive optics correction. Specifically relevant for GEO links with a point ahead angle of 18.5 μrad leading to a large displacement between the uplink and downlink path in the upper atmosphere.

The method implemented here is that described in 'Electromagnetic Wave Propagation in Turbulence' by Sasiela [31], initially a derivation is performed of losses without accounting for anisoplanatism. As a starting point, a Kolmogorov turbulence spectrum is assumed, similar to in the scintillation models used. Here, ignoring inner and outer scale effects,

$$\Phi_n(\vec{\kappa}) = 0.33C_n^2\vec{\kappa}^{-11/3}, 1/L_0 << \vec{\kappa} << 1/l_0 \tag{9}$$

which is only valid for the inertial range. However the assumption is made of a zero inner scale and infinite outer scale to simplify the analytical derivation. From Sasiela, the phase variance is given as,

$$\sigma_\phi^2 = 0.2073k_0^2 \int_0^L C_n^2(z)dz \int_0^\infty f(\kappa) \\ cos^2[P(\gamma,\kappa,z)]F(\gamma,\vec{\kappa})d\vec{\kappa}$$

where $f(k)$ is the turbulence spectrum. The Kolmogorov spectrum without inner and outer scale effects is then $\kappa^{-11/3}$. Furthermore ignoring diffraction and assuming a plane wave, allows the simplification of the diffraction parameter $P(\gamma,\kappa,z) \approx 1$. This equals assuming that the turbulence is all in the near field. Simplifying to a plane wave also gives the propagation parameter: $\gamma = 1$. The filter functions $F(\gamma,\vec{\kappa})$ can be used to isolate different contributors to the phase variance. Given that the tip-tilt is perfectly corrected, the tilt contribution and the piston must be removed, the later is not relevant for communication links. With the complex filter function of the piston and tip-tilt given as

$$G_P(\gamma\vec{\kappa}) = \frac{2J_1(\gamma\kappa D/2)}{\gamma\kappa D/2} \tag{10}$$

and

$$G_T(\gamma\vec{\kappa}) = \frac{4J_2(\gamma\kappa D/2)}{\gamma\kappa D/2}. \tag{11}$$

Giving the following expression for the piston removed phase variance:

$$\sigma_{\phi\ fig}^2 = 0.546\pi k_0^2 \int_0^L C_n^2(z)dz \int \kappa^{-8/3} \\ \left(1 - \left[\frac{2J_1(\gamma\kappa D/2)}{\gamma\kappa D/2}\right]^2 - \left[\frac{4J_2(\gamma\kappa D/2)}{\gamma\kappa D/2}\right]^2\right) d\vec{\kappa}, \tag{12}$$

where an angular integration is performed by replacing $\int d\vec{\kappa}$ by $2\pi \int \kappa$. Solving this for HV57 then approaches Equation 8.

F. Anisoplanatism phase variance

The effect of anisoplanatism is often not considered in link budgets, while low elevation angles and large point ahead angles would make the penalties quite significant for GEO links. Here, the anisoplanatic phase variance will be included by introducing another complex filter function,

$$G_{\vec{d}} = cos(L\kappa^2/2k_0)cos(z\kappa^2/2k_0) \\ -exp(i\vec{\kappa}\cdot\vec{d})cos((L-z)\kappa^2/2k_0)), \tag{13}$$

representing difference in phase of two propagation paths of length L separated by a distance d [31] . For an angle offset this results in the following filter function:

$$F_\theta(\vec{\kappa}) = sin^2\left(\frac{\kappa^2 z}{2k_0}\right) + 2cos^2\left(\frac{\kappa^2 z}{2k_0}\right)[1 - cos(\vec{\kappa}\theta z)] \tag{14}$$

The first sin term representing the amplitude impressed by the AO system, can be set to zero as only phase variance is being evaluated. The first cosine term is set to 1 by assuming again that diffraction is negligible. Giving the following,

$$\sigma_{\phi,\theta}^2 = 0.829\pi k_0^2 \int_0^L C_n^2(z)dz \int_0^\infty \kappa^{-8/3}\left[1 - J_0(\kappa\theta z)\right] d\kappa, \tag{15}$$

from this the piston component must be isolated,

$$\sigma_{\phi,\theta\ piston}^2 = 0.829\pi k_0^2 \int_0^L C_n^2(z)dz \int_0^\infty \kappa^{-8/3}\left[\frac{2J_1(\kappa D/2)}{\kappa D/2}\right]^2 \\ \left[1 - J_0(\kappa\theta z)\right] d\kappa, \tag{16}$$

in order to remove this from the total anisoplanatic phase variance to retrieve the effective phase variance [37].:

$$\sigma_{\phi,\theta\ eff}^2 = \sigma_{\phi,\theta}^2 - \sigma_{\phi,\theta\ piston}^2 \tag{17}$$

Subsequently using the extend Maréchal approximation to yield the resulting Strehl ratio of the total phase variance:

$$S = e^{-\sigma_{\phi,fig}^2} + e^{-\sigma_{\phi,\theta eff}^2} \tag{18}$$

G. Ansioplanatism pointing jitter distribution

The representation of tip-tilt corrected and anisoplanatism phase variance through the Strehl ratio provides a complete estimation of the mean turbulence-induced coupling loss. In this section this will be extended to include tip-tilt anisoplanatic induced fading probability density function. As given in Olivier et. al. [37] the phase variance induced by anisoplanatism as computed through Sasiela can be related to a one axis rms tilt as,

$$\sigma_{TA}^2 = \sigma_\phi^2 \frac{2}{\pi^2} \left(\frac{\lambda}{D}\right)^2 \tag{19}$$

This allows for a direct comparison to the analytical method given in Alaluf and Perdigues Armengol [38] in which Valley's [39] definition of decorrelation is used to express the tip-tilt rms wavefront tilt as a mean pointing jitter error σ_{TA}, with its associated losses as,

$$L_{j,\theta} = e^{(-4\sigma_{TA}/\theta_{div})^2} \tag{20}$$

The expression of the mean pointing jitter loss can be found to be mathematicaly equivalent to the extended Maréchal approximation by replacing σ_{TA}^2 in Equation 20 by Equation 19, and using $\theta_{div} = \frac{\lambda}{\pi w_0}$. Note however, that in Alaluf [38] the anisoplanatic losses are limited to anisokinetic phase errors, which means Equation 15 must be filtered for tip-tilt giving:

$$\sigma_{\phi,\theta\ tilt}^2 = 0.829\pi k_0^2 \int_0^L C_n^2(z)dz \int_0^\infty \kappa^{-8/3} \left[\frac{4J_2(\gamma\kappa D/2)}{\gamma\kappa D/2}\right]^2 [1 - J_0(\kappa\theta z)]\, d\kappa. \tag{21}$$

Which can be compared to Alaluf, showing good agreement of the mean tip-tilt anisoplanatic induced rms pointing error in Figure 4. Giving confidence in connecting the two methods.

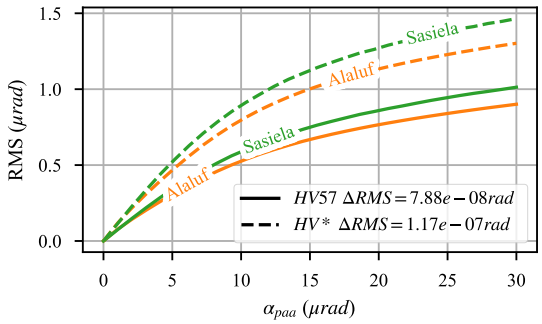

Fig. 4: rms phase tilt error for Alaluf and Sasiela method

Building on this representation as a jitter error it is possible to establish a distribution of this anisokinetic jitter error. Given that the tip and tilt Zernicke representation are Gaussian weighted for a Kolmogorov spectrum from Noll [27]. Also supported by the derivation of the extended Maréchal from the original Maréchal approximation by Ross showing how the extended Maréchal approximation is based on the assumption of a Gaussian distributed phase error [40]. The tip-tilt error thus consists of two identical orthogonal Gaussian distributed parameters, the radial combined pointing error θ_ϵ of which is given as a Rayleigh distribution:

elevation (deg)	w_0/r_0		θ_0/α_{paa}	
	HV57	HV*	HV57	HV*
90	0.37	0.71	0.67	1.12
70	0.38	0.74	0.75	1.24
50	0.43	0.83	1.04	1.72
30	0.56	1.08	2.06	3.40

TABLE II: Turbulence conditions, $w_0 = 7cm$ $\alpha_{paa} = 18.5\mu rad$

$$p(\theta_\epsilon) = \frac{\theta_\epsilon}{\sigma^2} exp(-\frac{\theta_\epsilon^2}{2\sigma^2}), \quad x \geq 0 \tag{22}$$

The standard deviation of this distribution is then found from the rms wavefront error $\sigma = \sigma_{TA}/\sqrt{\frac{\pi}{2}}$ and the pointing error associated with a radial pointing error θ_ϵ:

$$L_{s,\theta} = e^{-2\sigma^2/\theta_{div}^2} \tag{23}$$

This approach is suitable for a simple closed form approach to tip-tilt errors, due to anisokinetism or other sources. An alternative to the suggestion in Alaluf to use 1,2 or $3\sigma_{TA}$ to define a pointing loss given a confidence interval. Limitations of this simple expression implemented is the restriction to a distribution of tip and tilt modes. This approach of modelling the Zernicke modes as individual Gaussian distributed variables can also be extended to include higher order modes as well as non-isoplanatic scintillation. This method could be connected to the method of Schubert [41] with a Xi-squared distribution of the random Zernicke modes, and it indeed so that when reducing this distribution to tip-tilt, a Rayleigh distribution is obtained.

A methodology for the estimation of dynamic power losses in the link budget analysis of a feeder link has been presented, incorporating a distribution of expected turbulence conditions in continuous operations. With dynamic link methods, including the evaluation of scintillation and focused wavefront error losses, with a detailed derivation that accounts explicitly for anisoplanatic losses. Further deriving a simple analytical expression for the probability density function of anisokinetic losses in tip-tilt pre-correction systems. Initially, the results of these analytical phase losses wil be evaluated, as outlined by Sasiela. Followed by a comprehensive link budget analysis for communications to and from GEO and Tundra satellites, applying this methodology.

IV. Turbulence losses

This section will discuss the results of the analytical modelling approach of signal scintillation and beam coupling losses, explicitly including anisoplanatic errors. In addition to a mean loss the statistical margin required to maintain scintillation fades are compared for uplink geometries to GEO and Tundra.

A. Mean losses

Following the analytical model of wavefront phase variance, the Strehl ratio was computed using the Extended Maréchal

approximation. Giving coupling losses for a range of conditions representative for GEO and Tundra operations in Figure 5 with $D = 20cm$. Interpreting this figure, the $\alpha_{paa} = 0$ case considers mean coupling error losses for tip-tilt pre-compensation without anisoplanatic effects and, following the trend along the x-axis showing the effect of anisoplanatic losses due to the point-ahead angle. Note how for high link elevation angles of 50+ deg the mean anisoplanatic induced losses are limited to 0.5-1 dB. At low elevation angles, the compounding effect of increased atmospheric propagation path with mean losses can be observed with 1-2 dB induced losses by anisoplanatism.

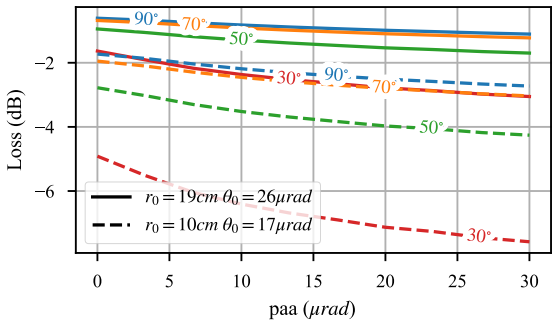

Fig. 5: Phase variance losses, including anisoplanatism for varying elevation angle and α_{paa}, $D = 20cm$

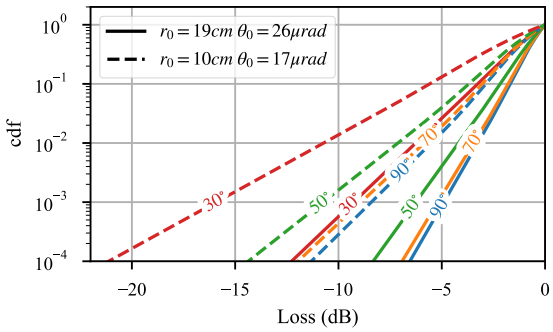

Fig. 6: CDF of signal fades, $\alpha_{paa} = 18.5\mu rad\ D = 20cm$

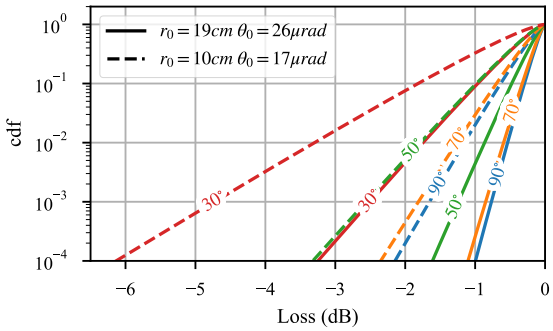

Fig. 7: CDF of tip-tilt anisokinetism signal fades, $\alpha_{paa} = 18.5\mu rad\ D = 20cm$

B. Scintillation losses

Following the same uplink configuration as for the mean signal coupling losses, results pertaining to signal scintillation are discussed. The cumulative distribution function (CDF) of the fading probability for varying link margins is presented in Figure 6. Similarly to the mean losses, the expected increase in turbulence effects for low-elevation links can be observed. Where for generally accepted fade probability of 0.01 under HV57 conditions, a GEO link at 30 deg would require a 7 dB scintillation fade margin. On the other hand a Tundra link at 50 deg would require a 4 dB margin. A considerable reduction which grows even more so under stronger turbulence conditions.

Due to the difference in the measured wavefront of the downlink to that of the pre-corrected uplink, tip-tilt jitter of the in-perfect tip-tilt AO correction will induce an additional anisoplanatism error. Implemented as a separate Rayleigh distributed CDF of the anisokinetic component Figure 7. Notable here is the stronger dependence on elevation angle than for ordinary scintillation. High elevation angle links show fewer losses even for stronger turbulence conditions than a 30 deg elevation link under HV57 conditions. Introducing an additional signal fade margin of -1.8 dB at 30 deg -0.5 dB at 50 deg for p<0.01 and HV57.

This impact of anisoplanatism on the mean losses and scintillation margin highlights the importance of considering these additional losses in system designs. This is particularly critical for low elevation uplink of GEO, which ought to include a mean 1 to 2 dB additional link margin as well as a 1.8 to 3.2 dB scintillation margin. Reinforcing the value of high link elevation angles due to the compounding effect of turbulence losses and reduced effectiveness of AO on the effective signal power. Notably, a loss which cannot be mitigated and is expected to increase with higher order AO compensation.

Comparing the projected losses to GEO at 30° and Tundra at 50° in average turbulence conditions (HV57), mean losses remain modest with -2.7 dB and -1.5 dB, respectively. Notable is that the improvements in mean phase variance losses alone sufficiently offset the additional free space losses encountered in Tundra orbits with 0.2 eccentricity. The robustness of the link to turbulence conditions considered in the 99% probability range requires an additional 4.3 dB link margin increase for GEO compared to 2.3 dB for Tundra. This is without considering the scintillation fade margin required.

V. Tundra Orbit Characteristics

The benefit of Tundra orbit often has theoretically been considered alongside highly-eccentric orbits for coverage of high-latitude regions, flight-heritage however is limited to the North-American Sirius-XM [42] and Japanese QZSS [43]. The following section will introduce general characteristics of Tundra orbits concerning geometry, radiation environment

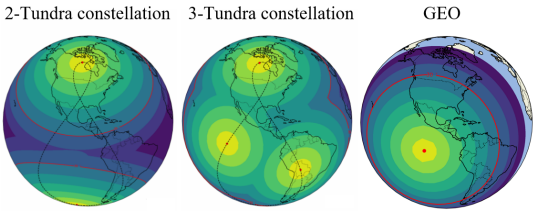

Fig. 8: Link elevation coverage snapshot

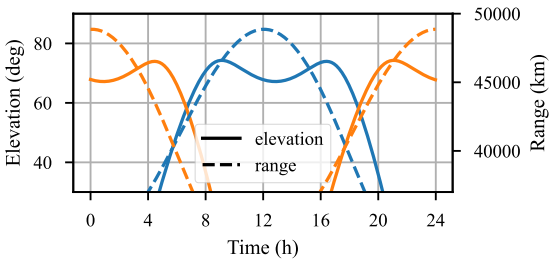

Fig. 9: Link Esquimalt (Vancouver, CA) to 2 Tundra e: 0.3 i: 63.4 deg

and ΔV costs. Addressing the general feasibility of this orbit as a GEO alternative and provide inputs for a subsequent orbit selection.

A. Link coverage and geometry

Geostationary orbits are characterised by their fixed position at the equator, as seen from an observer on Earth, due to a zero inclination and a period equal to Earth's rotation. Tundra orbits have a similar geosynchronous period. However, an observer on Earth will see the satellite rise to the zenith and fall over the horizon in the course of a day due to a slight eccentricity and a high inclination. The benefit of a Tundra orbit stems from its long dwell time over high-latitude regions, given an argument of perigee of 270 degrees and the non-zero eccentricity. This lower velocity at apogee, coupled with the rotation of the Earth, gives a Tundra ground track the characteristic loop at northern latitudes visible in Figure 21. The time a satellite spends above a desired latitude, notated as dwell time, can be related to the eccentricity and inclination of the orbit as [44],

$$DT = 1 - \frac{E - esin(E)}{\pi} \tag{24}$$

where E is the eccentric anomaly over a latitude

$$E = 2arctan\sqrt{\frac{(1-e)(sin(i)) + sin(lat.))}{(1+e)(sin(i)) - sin(lat.))}} \tag{25}$$

Where a GEO satellite has a continuous coverage of 1/3 of the globe, the coverage region of Tundra orbits will vary over time. Requiring at least two satellites to provide continuous coverage to the region of interest placed under the orbit apogee. Given a high-latitude coverage region such as Canada, a minimum elevation angle of 50 deg up to 60 deg latitude would be required (centralised in the coverage region); from geometry, this would require a satellite at geosynchronous altitude above 25 degrees latitude at all times. Thus requiring a dwell time of 50% and 33% above 25 deg latitude for a two and three satellite system covering this region, respectively. To provide adequately overlapping coverage as is illustrated in Figure 21. From Equation 25, inclinations under 40 deg can be excluded, and for the typical inclination of 63 degrees, this would require a minimum eccentricity of 0.25 for a two-satellite system and 0 for a three-satellite system. These general characteristics provide a good bound of the effective Tundra orbits for high-latitude coverage.

Considering the case of two Tundra satellites, in such a geosynchronous orbit, continuous coverage of high-latitude regions is possible. In Figure 9, the link geometry to Esquimalt, a proposed OGS location near Vancouver, CA, achieves a continuous coverage of 55+ deg elevation. Given that a link hand-over occurs twice a day such that the satellite with maximum elevation is active. With the varying link geometry over time, one could consider two limiting link cases for each ground station:

- **Satellite hand-over (ho)** - point of minimum elevation
- **Satellite at apogee (ap)** - point of maximum link range

Reviewing the effects of slant path on atmospheric effects and link length on signal spreading, there is a necessary balance between maximizing link elevation and minimizing range to effectively reduce both atmospheric and free-space losses for each of these limiting conditions. To consider these cases in Tundra orbit selection, the coverage performance is defined by the mean limiting path-losses over the region/points of interest, defined as:

$$L_{path} = L_{FSL,ap} L_{atm,ho} L_{Strehl,ho} L_{fade<0.01,ho} \tag{26}$$

Together with the previously defined atmospheric conditions, the mean and upper bound path-losses for each orbit providing acceptable dwell time can be considered.

B. Environmental effects

In designing and assessing a satellite orbit, it is important to understand the effect of the space environment on the operations and longevity of the satellite. A considerable challenge for orbits beyond Low Earth Orbit (LEO) is the radiation encountered when passing through the Van Allen belts and the reduced magnetic shielding beyond these protective rings [45]. Where the radiation and charging environment induces damages and anomalies due to radiation dosage, single-event upsets, and electric discharging. An evaluation of satellite anomalies has identified that, SEU accounts for approximately 28.4% of satellite anomalies, charging issues account for 54% of anomalies and TID damage accounts for 5.35% [46]. Highlighting the importance of proper environmental analysis in orbit design.

The radiation environment around the Earth is defined by the interaction between charged particles and the Earth's electromagnetic field. With in close proximity a high density of protons and electrons in the inner and outer Van Allen belt, respectively. Beyond the belts, a lesser density of high

energy Galactic Cosmic Rays (GCR) and solar particles can be found. The concern is that the eccentric nature of Tundra orbits could cause an elevated radiation environment during perigee in the Van Allen belts, and at apogee due to reduced magnetic shielding from solar and galactic particles at high inclinations.

The spacecraft radiation environment has been analysed for geosynchronous orbits providing sufficient dwell time to Northern latitudes. This analysis has been performed using the SPENVIS tool developed by ESA [47], following a methodology similar to that presented by Trichtchenko [48] in analysing highly-eccentric orbits. Implementing the following radiation sources:

- Trapped electron and proton particles
- Solar protons and heavy ions
- Galactic Cosmic Rays

Each orbit under consideration has been generated in SPENVIS for a trajectory of 1 year, over which the radiation sources and effects are computed. The effects of Earth shadowing and geomagnetic attenuation of the particles are adjusted accordingly by SPENVIS, with the Earth magnetic field lines defined by IGRF-13 for 2020. A mixture of solar and magnetic conditions represent mean or extreme conditions for each radiation source were relevant.

1) Trapped particles: The fluxes and spectra of the inner and outer Van Allen Belts are considered using the AE9 and AP9 (v1.50) dataset [49]. An empirical model well suited for inclined and eccentric orbits due to the inclusion of measurements by two HEO missions [48]. The analysis of each orbit consists of the mean of seven orbits spaced at 60 deg RAAN to average out longitudinal variations in the Van Allen belts. Moreover, providing generalised results applicable to an entire constellation, irrespective of launch epoch or orbit RAAN. The mean proton and electron density are evaluated to provide long-term predictions of the total ionisation dose. The movement of satellites in three geosynchronous orbits has been illustrated in Figure 10, showing the pass through the outer radiation belt. An eccentric orbit is notably exposed to higher peak fluxes however, for a shorter duration. Note that AP8 andAE8 have been displayed in Figure 10 due to functionality limitations in generating a coordinate frame in SPENVIS.

2) Solar protons and heavy ions: Charged particles ejected by the Sun provide mean and peak fluxes to a satellite beyond the Van Allen Belts shielding. The mean ionisation impact of solar protons and solar heavy ions (H to U) has been modelled with ESP [50] and PSYCHIC [51], respectively. Evaluated during solar maximum with a quiet magnetosphere and a confidence level of 95% that this cumulative fluence of solar events is not exceeded. The peak solar particle flux, for a5min worst-case SEU analysis follows from CREME-96 [52], a dataset representing the worst week and worst 5 min averaged peak flux during the 1989 October solar flare, considered a 99% confidence-level worst-case event.

3) Galactic cosmic rays: Galactic Cosmic Rays conditions are likewise based on CREME-96 and corresponds to measurements of the last maximum of GCR observed in 1986-87. Corresponding to solar minimum conditions with reduced solar magnetic shielding, thereby increasing the intensity of Galactic Cosmic Rays observed in the heliosphere.

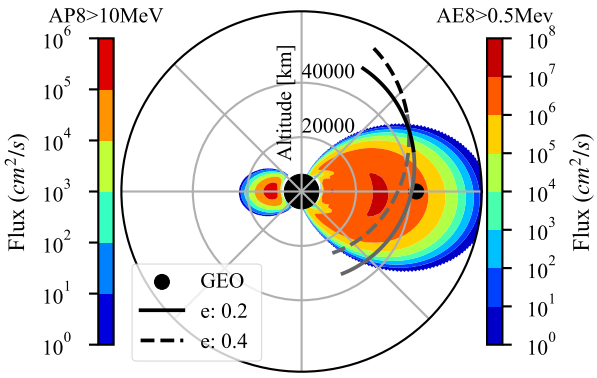

Fig. 10: Trapped particles flux AP8 (left) and AE8 (right)

4) Total ionisation dose: The total ionisation dose integrated over a year could be determined using the SHIELDOSE-2 model [53] for a Silicone material shielded by a finite Aluminium slab. The ionisation effect of trapped particles, solar protons and Bremsstrahlung is considered. An aluminium shielding of 3mm thickness was taken, equivalent to the required shielding in GEO, to achieve an acceptable 5krad yearly dose. The resulting radiation dosage over the design space of Tundra orbits is then explored in Figure 11. The trapped proton effects of the inner Van Allen Belt have been omitted from this overview as these have been found not to affect high-altitude orbits.

The passing of eccentric and inclined orbits through the outer Van Allen Belt illustrated previously in Figure 10 results in a change in cumulative dose effect due to an increased intensity of electrons deeper in the belt. Large inclination orients the perigee more to the south pole and avoids more significant portions of the outer belt to reduce the integrated dose. Larger eccentricity results in higher radiation doses, as the reduced transit time through the outer belt does not compensate for the increased radiation flux from a deeper pass. As a secondary effect of electron penetration in aluminium, Bremsstrahlung shows little contribution to the overall dose and follows the same relationship to orbit geometry as that of trapped electrons. Solar proton dose shows close to no variation from orbit to orbit, with little magnetic shielding variations for such high-altitude orbits. Unlike in LEO, no increased solar particle densities are experienced by inclined orbits passing over the polar regions, agreeing with other research [54]. The reduction in Solar proton TID, which is visible at high eccentricities, can be explained by the shielding effect of the Outer Van Allen Belt. In which the deeper pass through this belt shields the highly eccentric orbit from solar particles. The effect however, is quite limited. The aggregated TID of the Tundra orbit options compare favourably to the yearly 5 krad dose of GEO, with the classical Tundra orbit

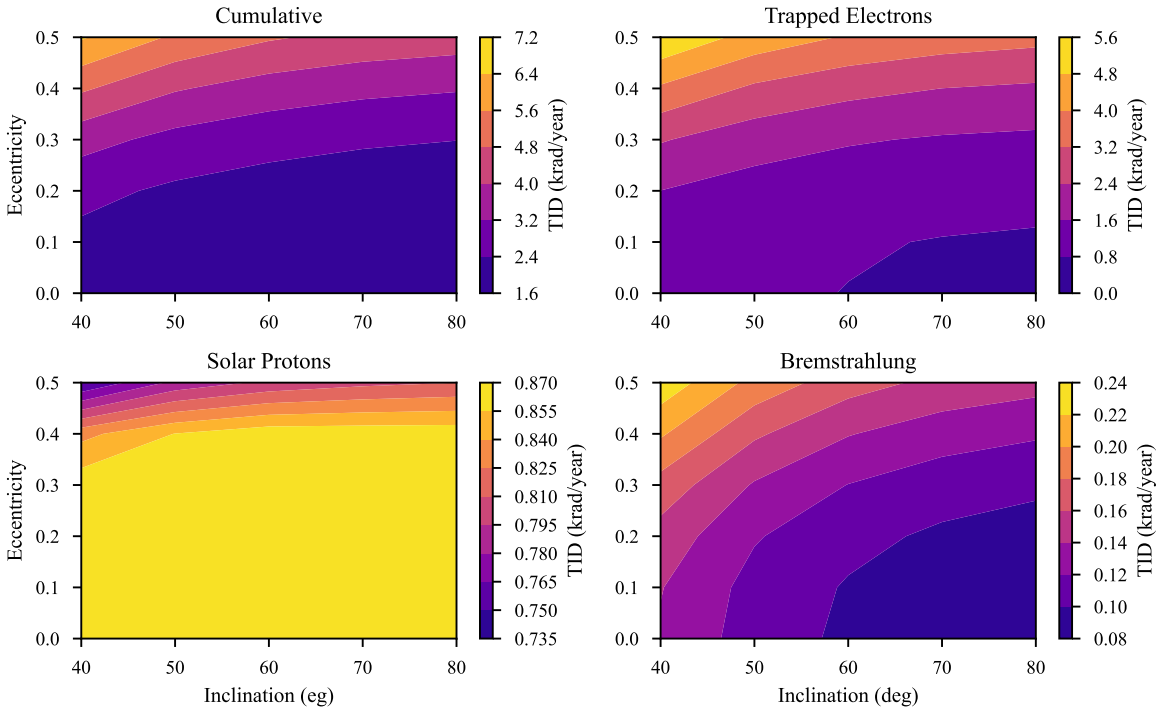

Fig. 11: Yearly Total Ionisation Dose for Geosynchronous orbits

of 0.2 eccentricity and 63 deg inclination with a 58% lower dose.

5) Single Event Upsets: The likelihood of SEU has been assessed by estimating the SEU rates using a default SPENVIS Silicon device under 4mm Aluminium shielding. This analysis incorporates a worst-case scenario of a 5-minute intense particle radiation exposure typical in various orbital environments. The calculation includes contributions from solar particles, trapped protons, and GCR. It is important to note that the device used in this analysis serves as a standard benchmark to identify relative differences across orbital paths rather than providing absolute SEU rates. The difference in SEU in Figure 12 shows little variations over orbits, as was visible in Solar proton TID. The protective geomagnetic shielding effect is only significant for a high inclination orbit of 0.4+ eccentricity.

6) Deep charging: Charging is identified as the root cause of more than 50% of satellite anomalies, necessitating a first-order approximation of its effects. Detailed analysis of charging effects is left for future analysis, requiring detailed knowledge of the spacecraft materials and properties. Deep transits through the electron belt pose a risk of internal deep dielectric charging due to high electron flux intensities. A 'safe' threshold of penetrating radiation has been established at a mean 10h flux of 10^5 $electron/cm^2/s$ [55]. This threshold is particularly critical for satellites in eccentric orbit, which frequently pass through region of heightened fluence in the outer Van Allen Belt. The penetrating electron flux has been analysed using the MFLUX tool in SPENVIS, with AE9 electrons at a 95% confidence interval with $1g/cm^2$ (3.7mm) aluminium shielding. For a GEO satellite, the reference shielded flux was computed to 1.04e5 $electron/cm^2/s$, slightly above the established safe limit. It was observed that the majority of Tundra orbits exceed this margin considerably. Notably, orbits with a low eccentricity and high inclination benefit from the shorter exposure times within the radiation belt and avoiding passing through higher electron density areas. Subsequent analysis of increased aluminium shield of $2g/cm^2$ was able to achieve penetrating fluxes far below the required threshold.

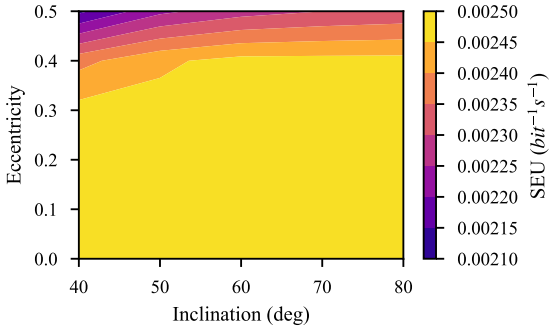

Fig. 12: Single Event Upset 5 min worst case

7) Surface charging: Surface charging occurs due to satellite surface interaction with plasma and solar UV; causing the surface to adopt a charge that balances the net current. This

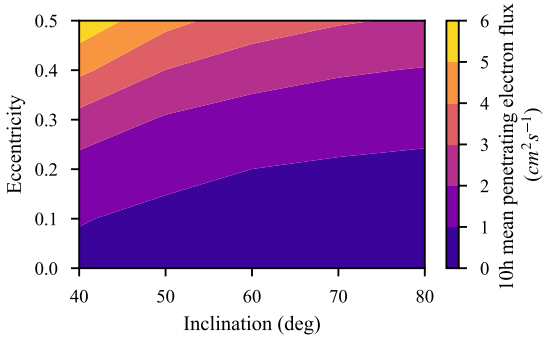

Fig. 13: Shielded electron flux, 10hour mean

interaction varies due to differences in materials, shadows, and plasma conditions, leading to varying surface potentials that may cause electronic discharges into space. Analyzing surface charging is highly complex, as it depends on the specific satellite configuration and the surrounding charging environment. Consequently a qualitative assessment of the trends in the design space of interest is presented here. Equatorial orbits, and GEO specifically, are under the influence of sub-storm plasma injections. The periodic re-connection of the plasma-sphere tail at the Earth's midnight side generates a movement of energized ions and electrons towards Earth. This cloud of electrons circulates westward along Earth's magnetic field lines, reaching geostationary altitudes primarily at the midnight and noon positions and causing the majority of the charging events. Such electron dynamics also apply to highly elliptical orbits, which intersect the geosynchronous altitude magnetic field line between 00:00 and 06:00h, as documented by Fennell [56]. This evidence suggests that Tundra orbits, traversing similar altitude, are likely to experience comparable charging events.

In conclusion, an comprehensive examination of environmental effects on Geosynchronous satellites has highlighted the similarities and differences between Tundra and GEO orbits. Notably, Tundra orbits demonstrate a significant mean reduction of 40% in Total Ionization Dose compared to GEO. However, a pronounced vulnerability to deep electric charging is observed in Tundra orbits with eccentricities exceeding 0.2, attributed to more frequent and deeper passes through the electron belt. Noting however that increased shielding effectively mitigates low energy electron penetration. Magnetic shielding effects appear to have minimal impact, with only negligible variation in solar proton dose and particle induced SEU rates (+-5%). Nevertheless, there is a marginal reduction in SEU rates at higher eccentricities, although these orbits are less favourable due to increased risks associated with deep charging. While surface charging effects have not been explicitly analyzed in this study, insights from measurements in highly elliptical orbits suggest that the environment in Tundra orbits would resemble closely to that of sub storm charging events in GEO. From our findings a significant number of inclined and moderately eccentric Tundra orbits demonstrate environmental performance that is comparable, if not superior, to that of GEO orbits. The reduced TID in these orbits potentially allows for the downsizing of solar arrays, as less robust shielding against radiation damage and charging may be required, thus impacting both the cost and weight of future VHTS.

TABLE III: Tundra 2 year orbital elements variation [58]

Element	Typical var.	Maximum var.
e	0.03	0.07
i	0.5 °	1.2 °
ω	6 °	15 °
Relative RAAN	1 °	3°
Absolute RAAN	9 °	11°
LAN	100 °	150 °

C. Orbit control

Under the influence of various perturbations including Earth, lunar, and solar gravitational fields, as well as solar radiation pressure and atmospheric drag, satellite orbits experience alterations in their trajectories. The primary objective of orbit station keeping is to maintain a stable orbit or consistent ground track throughout the mission's duration. For high-altitude Tundra orbits, the orbital perturbations can be effectively summarized by three main factors with sufficient accuracy, as identified by Bruno and Pernicka [57]: J2 (Earth's oblateness) perturbation, lunar gravitational perturbation, and solar gravitational perturbation. These perturbations exhibit a biennial cycle in relation to the right ascension of the ascending node (RAAN) of a satellite, leading to varying evolution across satellites within a constellation.

To address these variations, Fantino et al. [58] generated a set of typical changes in Tundra orbital elements over a two-year period. This data has been utilized in this study to derive generalized estimates for the ΔV costs necessary for effective station keeping. The orbit control costs are calculated using the rewritten expressions of the Meirovitsch formulation by Bruno [57] and the typical variation of orbital elements as presented in Table III. The contributions of semi-major axis and longitude-of-ascending-node (LAN) control are deemed negligible in our computations (less than 1 m/s per year), despite their importance in maintaining correct geosynchronous phasing with the coverage region. While a GEO satellite is required by regulation to adhere to strict station keeping in its allocated orbital slot, Tundra orbits could make use of ΔV cost saving station keeping strategies. The following station keeping strategies are relevant for Tundra orbits:

- Orbital elements control: A traditional station keeping approach where all orbital elements are controlled to preserve the exact orbit geometry. In this adaptation, RAAN control is relaxed by only maintaining relative phasing within the constellation [58]. This the most costly approach which for typical perturbations in Table III would result in an approximate 66 m/s yearly ΔV cost.
- Ground-track control: Leveraging the periodic nature of third-body induced inclination and eccentricity variations,

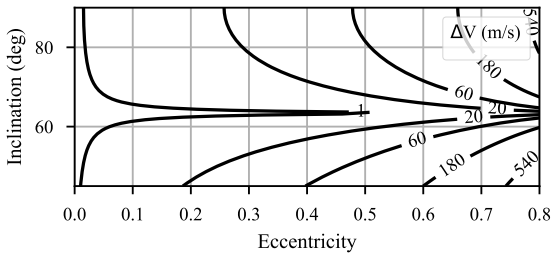

Fig. 14: Perigee J2-ω Δ (m/s)

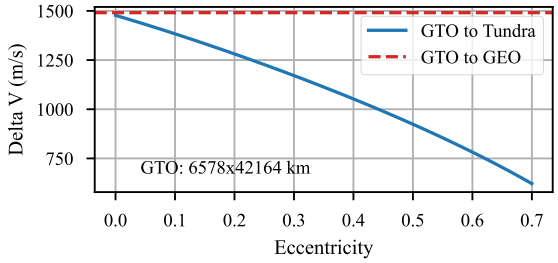

Fig. 15: Impulsive insertion from GTO

the orbit is only controlled through argument of perigee, RAAN and semi-major axis corrections[58], resulting in 39 m/s yearly ΔV.

- East-West control: Proposed by Jenkin et al. [59], this strategy involves minimal control, allowing the orbit to evolve freely over its lifetime and only perform East-West station keeping. Long term propagation shows that the coverage of the high-latitude region of interest is maintained to an acceptable degree. Given a constellation, in which relative RAAN spacing is maintained, a yearly budget of just 19 m/s would be required based on Table III, in addition to very limited cost for semi-major axis corrections for East-West positioning.

With the above generalized budgets based on typical results and orbit control maneuvers computed for a classical Tundra orbit, there is an opportunity to perform orbit optimization to balance perturbing forces and minimize orbit evolution. The typical frozen orbit is identified by minimizing the Earth's J2 perturbation, which is influenced by the Earth's larger radius at the equator leading to rotation of the argument of perigee. The J2 effect varies with orbit inclination angle, as illustrated in Figure 14, with no argument of perigee rotation occurring at the frozen inclination of 63.4 deg. This inclination corresponds to the classical Tundra orbit (inclination 63.4, eccentricity 0.268) for which the station keeping requirement 61 m/s per year [57]. Bruno and Pernicka [57] further refined the positioning of these frozen orbits and utilised the perturbing effects of third-body influences to generate alternative frozen constellations, thereby reducing the required ΔV to 24 m/s annually.

In conclusion, this analysis of station keeping requirements for Tundra orbits highlights a range of viable strategies that offer competitive performance with respect to the 44 m/s annyal station keeping costs for GEO. The diverse approaches, from orbital element control to ground-track and East-West control, demonstrate significant potential for ΔV cost savings.

D. Insertion and End-of-life

A first order comparison of the required manoeuvre cost at beginning and end-of-life can be considered using ideal impulsive transfers. Assuming a launch vehicle insertion to a Geo-Transfer-Orbit (GTO), which for GEO is in a 5° inclined orbit (Kourou launch) and for a Tundra orbit directly in the required orbit inclination. Derived from the basic principles of a Hohmann transfer, a more eccentric orbit reduces the necessary apogee burn while increasing the more efficient perigee burn (Figure 15).

However, this initial benefit of more eccentric orbits is offset by the required end-of-life (EOL) strategy. Eccentric orbits undergo lunar-solar perturbations, notably resonating the eccentricity of the orbit, which could lead to atmospheric re-entry and incursion into satellite-dense regions. These variations are a function of the initial RAAN relative to the Sun and Moon and orbit inclination, varying across satellites in a constellation. The EOL strategy must serve the purpose of minimising collision risk with active and inactive objects, clearing protected regions, and ensuring an orbital lifetime of $<$200 years. Following the Tundra disposal study [60] the following disposal strategies and long-term characteristics ar considered:

- Near-Tundra disposal orbit: Raise semi-major axis by 376km to clear the operational orbit, comparable to GEO EOL strategy. This approach provides a large RAAN-inclination space with an orbital lifetime of less than 200 years. However, it does not clear GEO the collision probability with objects is 3e-6 and 5e-7 for active and inactive objects respectively.
- Apogee Lowering to 486 km below GEO: Lower apogee to clear the GEO protected region. Only a small RAAN-inclination space with lifetime of $<$ 200 years, which however does clear GEO. Slightly higher collision probability of at most 3e-5 and 5e-6.
- Circularise at perigee: Circularise by lowering apogee altitude, to reduce solar and lunar effects. Lifetime exceeds 200 years for all RAAN-inclination, clearing GEO protected region. Highest collision probability of maximum 8e-5 and 5e-6.
- Circularise at apogee: Circularise by raising perigee altitude, reducing solar and lunar effects. Lifetimes ranging from less than 50 to over 200 years. Adjustments to the argument of perigee can clear the GEO belt, with collision probabilities of up to 4e-5 and 5e-6.

Each EOL strategy consists of a two-burn sequence at apogee and perigee, with varying costs based on eccentricity as depicted in Figure 16. Note that additional maneuvers to minimize orbital lifetimes by adjusting RAAN or argument

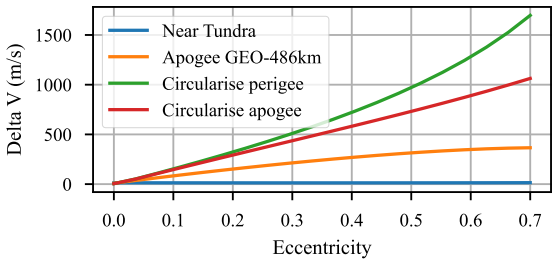

Fig. 16: End-of-life manoeuvre dv

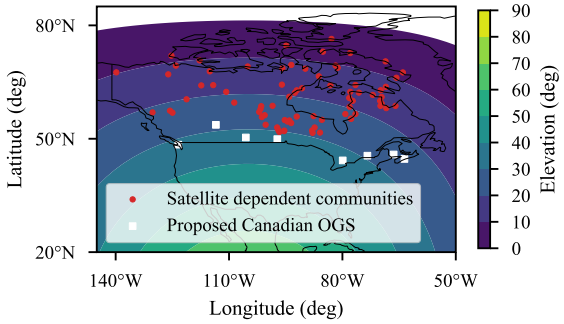

Fig. 17: GEO (105°W) link to Canada

of perigee are not included, as these will vary from satellite to satellite within a constellation.

The Near-Tundra disposal strategy emerges as the most effective, requiring the lowest ΔV. While it does not clear the GEO region, it has the second-lowest overall collision probability. However, due to variations in the eccentricity of the disposal orbit, it is uncertain if the results by Jenkin for an eccentricity of 0.26 can be generalized to larger eccentricities. Circularisation at perigee is the only strategy which ensures clearing of the GEO protected region for the entire RAAN-inclination space, although this is the most expensive in terms of ΔV.

The EOL strategy for GEO in contrast requires orbit raising to a circular stable graveyard orbit 300km higher, requiring just 11 m/s of ΔV. A classical Tundra orbit (e:0.26) would theoretically economise 210 m/s during insertion and for low eccentricity orbits the near-Tundra orbit disposal would incur two additional manoeuvres totalling just 13 m/s. In this scenario Tundra orbits would significantly reduce ΔV costs. That said, with the stability of near-Tundra disposal not investigated for higher eccentricities and the possibility of requirements restricting GEO region incursion, the more expensive orbit disposal by Circularisation at perigee must be considered as well. This latter option would require a perigee burn of 323 m/s. Giving an EOL cost that increases with orbit eccentricity, effectively outweighing the savings achieved during orbit insertion

VI. Canada case study

A case study was conducted to examine the application of Tundra orbits for enhancing coverage across Canada and integrating with a domestic optical ground station network This analysis focuses on the performance of optical feeder links to a Very High-Throughput Satellite system, utilizing a network of nine OGS sites confined to Canadian territory as outlined by Gagnon et al. [61], achieving a cloud-free line-of-sight availability of 92.9%.While this is insufficient for general optical feeder links QOS, this network is assumed for a baseline comparative analysis of Tundra orbits implementation. Yet, it is noted that expanding this network, as demonstrated by similar high-latitude OGS networks in Europe - including cities like Oslo, Berlin, and Birmingham - could potentially increase availability to 99.5% for 11 OGS [8].

Connecting these Canadian OGS sites to VHTS in GEO poses significant challenges due to the low elevation angles encountered at high-latitudes, as depicted in Figure 17. These challenges have been detailed through a link budget analysis from the Esquimalt ground station at 48.44deg N 123.34deg W in Table IV, highlighting the impact of this low link elevation angle. Gagnon et al. recognise the challenge of this GEO-ground link at high-latitudes and suggest alternatives such as OGS abroad and GEO-HAP (High Altitude Platform) links [62].

Optical feeder links located in Canada could benefit from the effective high-latitude coverage of Tundra orbits, not necessitating the deployment of OGS abroad or the deployment of expansive LEO constellations with global coverage. The selection of a suitable Tundra orbit for a two and three satellite constellation for coverage of this OGS network ahs been done. Additionally considering the coverage of satellite-dependent communities in Canada [63] as a possible use-case with Tundra VHTS providing backhaul or broadband connectivity. The scope of this us case includes a preliminary coverage analysis for these user links. Comprehensive performance evaluations of these links are left for future analysis.

A. Orbit selection

The orbits are to be optimised for the OGS network under evaluation. For such a geosynchronous orbit, the semi-major axis is naturally fixed at 42,164.7 km, and as outlined in Equation 25, an argument of perigee of 270 degrees is chosen to maximize satellite dwell time over Northern latitudes. The longitude of the ascending node is chosen at 270 deg for an apogee centered in Canada. The configurations under analysis are then: a two satellite constellation and a three satellite constellation, with orbital planes and mean anomalies evenly phased. This arrangement leaves eccentricity and inclination as the primary variables to be determined. In selecting an orbit for these constellations, our criteria are as follows:

1) Maximization of optical link performance: The orbit must enhance the performance of optical links, increase data rate and availability across the coverage region.
2) Feasibility and competitiveness relative to GEO: Maintain orbit cost and environment as good as GEO or with minimisation of the required mitigation's.

TABLE IV: GEO - mean link budget to Esquimalt

Parameter	Uplink	Downlink
Link length (km)	38467	38467
Elevation angle (deg)	31.6	31.6
Point ahead angle (μrad)	18.5	0
Tx beamwaist (cm)	7.1	8.8
Tx power (dBm)	47	30
Tx antenna gain (dB)	112.2	114.1
Tx optical loss (dB)	-3.0	-3.0
Tx jitter pointing loss (dB)	-1.6	-2.5
Free-space loss (dB)	-289.9	-289.9
Absorption loss (dB)	-0.86	-0.86
Scintillation p<0.01 (dB)	-5.1	-4.7
Mean Strehl (dB)	-1.6	-2.2
Mean anisoplanatism loss (dB)	-1.0	0
Scintillation ani. p<0.01 (dB)	-1.6	0
Rx diameter (cm)	25	50
Rx antenna gain (dB)	114.1	120.2
Rx optical loss (dB)	-3	-3
Total Rx power (dBm)	-35.4	-42.0
Link margin (dB)	3	3
Target BER ()	e-9	e-9
Ideal data rate BPSK (Gbs)	122	21

GEO - 99% turbulence link margin to Esquimalt

Parameter	Uplink	Downlink
Scintillation p<0.01 (dB)	-9.0	-8.0
Mean Strehl (dB)	-4.7	-6.8
Mean anisoplanatism loss (dB)	-2.0	0
Scintillation ani. p<0.01 (dB)	-3.1	0
Unmitigated data rate (Gbs)	9	2
Required margin w.r.t. mean (dB)	11.5	7.8

Firstly the coverage performance of different orbits is presented. Followed by a discussion on environmental factors and ΔV constraints to narrow down the design space. Before concluding with a focused optimization of the link parameters.

1) Coverage: For each orbit the link geometry to the ground station in Figure 17 has been generated, storing link length and link elevation angle offered by the two and three satellite constellation. From this the limiting link for each location, representing longest link length (at apogee) and lowest link elevation (at handover) is considered as performance indicator. The minimum and mean of these OGS limiting links are presented in Figure 18 and 19. From this analysis, the following predictable results are visible: higher eccentricity orbits tend to increase both the mean and limiting elevation angles. Particularly beneficial for satellite dependent communities which are spread across higher latitudes, with the most northern community Grise Fiord located at 76 degrees latitude. These findings indicate that, across all evaluated cases, the optimal inclination for maximizing coverage lies between 55 and 75 degrees and with a maximisation of eccentricity favoured.

2) Orbit environment: The evaluation orbital environment of Tundra orbits provides limits to the sustainable operations in these orbits without requiring significant modifications from GEO-rated hardware. From the coverage maps, the optimal inclination angles for Tundra orbit coverage also fall within the favourable regions in order to minimise the incursion of the outer Van Allen Belt, lowering TID and deep charging effects. These results do however, highlight the risk of deep electric charging at high eccentricities beyond 0.3. Conversely, orbits with eccentricities below 0.2 demonstrate substantial improvements in these respects when compared to traditional GEO operations. Based on these insights, the inclination-eccentricity design space for Tundra orbits can be sustainably maintained up to an eccentricity of 0.3 (depending on inclination angle, see Figure 13), offering a viable range for sustainable long term satellite operations.

3) Orbit ΔV characteristics: Orbit insertion, EOL and station keeping cost provides a metric to constrain the design space. In the absence of long-term numerical propagation and details on launch date a general argument on orbit ΔV costs is made.

For orbit control costs, a ground-track-only maintenance strategy is chosen. Maintaining stable phasing and argument of perigee, while allowing eccentricity and inclination to vary. This approach permits the satellite coverage to evolve within the coverage plots provided with eccentricity and inclination. The maximum two year variation, 0.07 in eccentricity and 1.2 deg in inclination, is expected to have minimal impact on coverage.

From Figure 14, the inclination of 63.4 degrees clearly minimizes the required yearly control of perigee positions due to the J2 perturbation. Additionally, third-body effects might allow for the selection of frozen orbits based on individual orbit RAAN-inclination-eccentricity combinations. While such orbits offer reduced ΔV costs for maintenance, these would also potentially maintain prolonged stability in their graveyard orbits, failing to de-orbit within the prescribed 200-year period. Consequently, due to time constraints and the required coupled analysis of long-term operation and EOL stability, this strategy has not been pursued. Subsequently the design space has been limited to the J-2 frozen orbit 63.4 deg inclination, which is a good compromise from the optimal inclinations in Figure 18 and 19.

Orbit insertion and EOL exhibit slight variations, favoring lower eccentricities or higher eccentricities depending on the employed EOL strategy. Since orbits are inserted into their respective planes via separate launches, inclination does not significantly impact orbit insertion costs. Higher eccentricity does however benefit the efficiency of the impulsive manoeuvres. If one would consider the Near-Tundra Orbit strategy, this benefit for eccentricity stands. However, if there is a strict de-orbit and GEO clearing requirement the circularisation at apogee would on the other hand benefit eccentricity. Consequently pending such detail this is considered as a neutral argument in orbit selection.

4) Link optimisation: The evaluation of orbit implementation consideration have restricted the design space to an inclination of 63.4 degrees, while limiting the eccentricity to a maximum of 0.3. To optimise the remaining variable eccentricity for the intended coverage region, the limiting link losses are evaluated as detailed in Equation 26. The bounds for average conditions and 99% turbulence levels, assuming an atmospheric attenuation of 0.45 dB, have been computed for varying eccentricity. The results of this analysis are depicted in

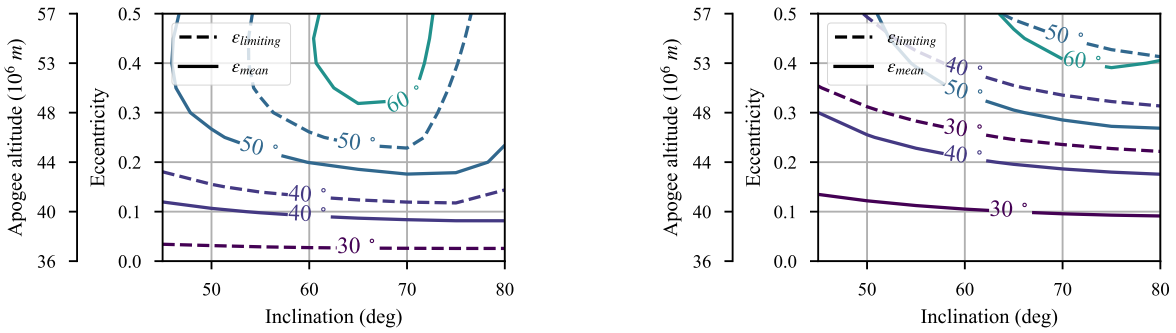

(a) Limiting link to OGS

(b) Limiting link to Satellite Dependent Communities

Fig. 18: Limiting coverage for Tundra 2 satellite constellation

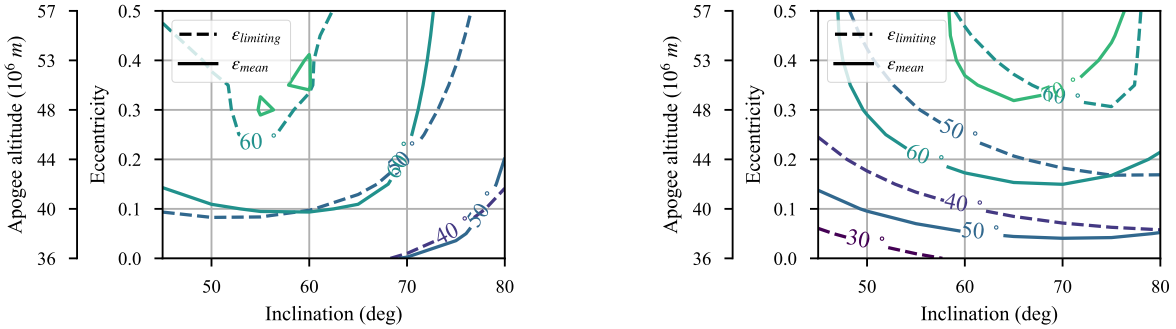

(a) Limiting link to OGS

(b) Limiting link to Satellite Dependent Communities

Fig. 19: Limiting coverage for Tundra 3 satellite constellation

Figure 20, which illustrates the evolution of limiting link loss across the two sets of coverage locations. From this analysis, orbits have been chosen to minimise link losses to the OGS network at 99% conditions, giving:

- For the two satellite array: An eccentricity of 0.3 and an inclination of 63.4 degrees
- For the three satellite array: An eccentricity of 0.2 and an inclination of 63.4 degrees.

It is notable that the difference in link losses between the two configurations for the OGS network is minimal. Additionally, the configuration with three satellites exhibits quite stable bounds for links to satellite dependent communities for the entire range of eccentricities making it particularly suitable for extensive coverage areas.

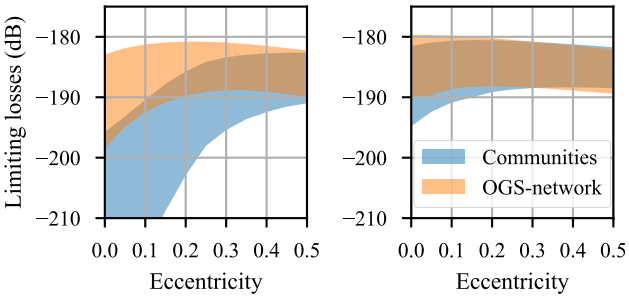

Fig. 20: Limiting link losses(2 sat left, 3 sat right)

B. Orbit results

The following section details the orbit characteristics of the selected Tundra orbits in comparison to a Geostationary satellite situated at 105 deg West. The general characteristics are summarized in Table VI. The two Tundra constellations selected provide excellent coverage and elevation angles over the optical ground stations locations and the satellite-dependent communities under consideration. In Figure 21, the minimum link elevation across the coverage region are presented, complemented by skyplots for the OGS at Esquimalt located on the Canadian west coast. This visualization illustrates the effective field of view from the OGS.

Clear improvement in link elevation angles are visible compared to GEO. It is interesting to note the marginal elevation angle improvements from the two to three satellite coverage of the OGS. Where in the two satellite configuration the increased eccentricity helps improve the coverage however, at the cost of additional free-space losses.

The pointing data from Esquimalt indicate acceptable az-

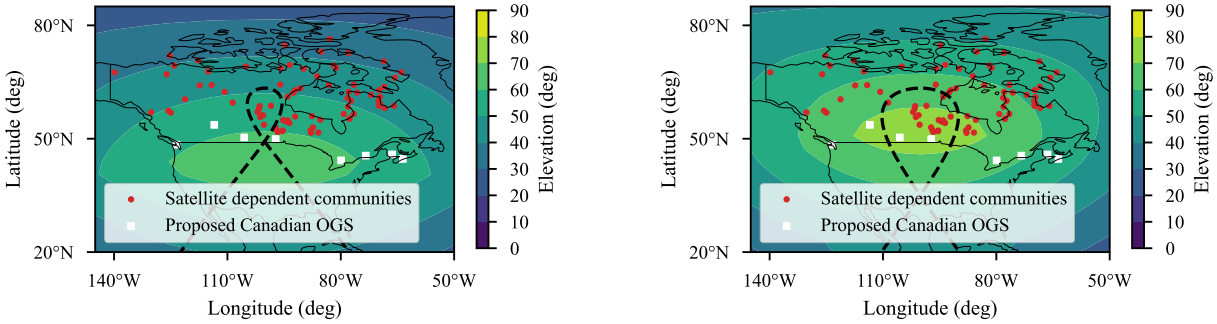

(a) Minimum elevation Tundra 2

(b) Minimum elevation Tundra 3

Fig. 21: Link elevation

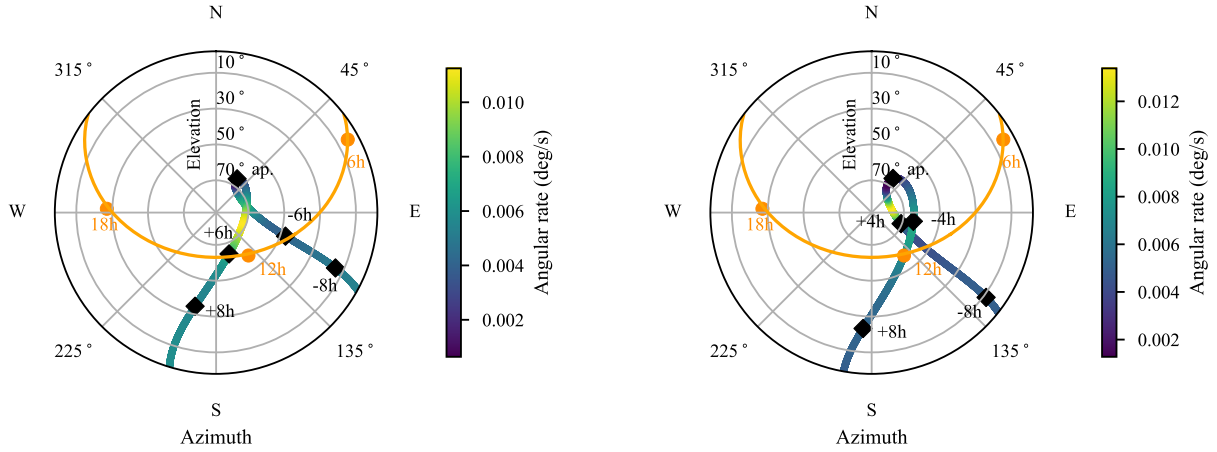

(a) Skyplot Esquimalt Tundra-2

(b) Skyplot Esquimalt Tundra-3

Fig. 22: Skyplots with angular rate and Sun path in UTC-7 (orange)

TABLE V: Coverage summary

Orbit characteristic	GEO 105°W	Tundra 2	Tundra 3
OGS coverage			
mean elevation (deg)	29.5	70.2	70.7
min elevation (deg)	24.3	53.6	54.6
Oneway latency (s)	0.13-0.13	0.12-0.16	0.13-0.15
max azimuth rate (deg/s)	0	0.041	0.056
max elevation rate (deg/s)	0	0.004	0.036
Satellite dependent communities coverage			
mean elevation (deg)	18.6	71.1	74.4
min elevation (deg)	3.9	34.6	48.8
Oneway latency (s)	0.13-0.14	0.13-0.16	0.14-0.15
max azimuth rate (deg/s)	0	0.048	0.121
max elevation rate (deg/s)	0	0.004	0.004

TABLE VI: Orbit characteristics summary

Orbit characteristic	GEO 105°W	Tundra 2	Tundra 3
Semi-major Axis (km)	42164.7	42164.7	42164.7
Eccentricity	0	0.3	0.2
Inclination (deg)	0	63.4	63.4
Argument of Perigee (deg)	-	270	270
LAN (deg)	-	270/90	270/150/30
Mean Anomaly (deg)	-	0/180	0/120/240
ΔV control (m/s/year)	44	41	34
ΔV insertion (m/s)	1491	1171	1281
ΔV end-of-life (m/s)	11	13/436	13/293
TID (krad/year) 3mm Al	5.1	2.7	2.1
SEU (/bit/s) 5min worst case 4mm Al	0.0025	0.025	0.025
Penetrating flux ($/cm^2/s$) 10h mean 3.7 mm Al	1.04e6	1.28e6	0.82e6

imuth and elevation rate throughout the apogee pass. Notably, there were no significant accelerations due to changes in relative direction at the apogee. In Figure 22 the time relative to apogee is included, to be used to see the separation of the satellites in the constellations. Whereas for a two satellite constellation, this separation at handover is relatively large, for a the three-satellite constellations it is notably small. This hints at the possibility of tuning the orbit loop for near-seamless satellite handover. However, in practice step wise handovers can be implemented trough multiple pointing architectures, giving fractional throughput losses during satellite handover periods.

A critical concern for optical communications is the Sun

angle, where small angles increase background noise and could potentially damage sensitive equipment. The Sun path during the June equinox - highest pass at the northern latitude - has been included. Close approaches between the satellite and Sun path could be mitigated through strategic phasing, such as positioning the apogee at noon or planning handovers in the morning or afternoon. This does, however, require control of the mean RAAN motion of the constellation. Phasing the daytime orbit for an apogee at 12h is also interesting from a turbulence mitigation perspective due to the diurnal variation.

A final differentiation factor between GEO and Tundras is the point ahead angle, which, as outlined in Equation 3, increases with tangential orbital velocity. The varying velocity in Tundra orbits causes this value to fluctuate from 18.2-15.1 μrad for two satellite and 17.9-16.7 μrad for a three satellite array from handover to apogee, reaching its minimum at apogee.

Based on our analysis of the orbit characteristics, it is clear that the selected Tundra orbits provide significant improvements in coverage, albeit with the requirement of deploying two or three satellites. Environmentally, these orbits are viable, maintaining acceptable radiation levels with minimal mitigation required for 0.3 eccentricity orbits to protect against deep charging effects encountered during daily transits through the outer Van Allen belt. From a geometrical standpoint, the pointing requirements for Tundra orbits pose no significant challenges and sun-exclusion can be performed comparatively simply and effectively. Accommodations will have to be made for satellite handovers by the distribution of Tx and Rx apertures over separate pointing systems to minimise loss of instantaneous throughput.

C. Link budget results

An up- and down-link link budget for the Esquimalt ground station at 48.44 deg N 123.34 deg W is presented for the ordinary GEO (Table IV), two satellite Tundra and three satellite Tundra constellation in Table VII-X. These link budgets include the mean expected atmospheric conditions as HV57, followed by a budget for the required link margin to operate in 99% confidence turbulence conditions.

Under average conditions, the Tundra constellations show significant improvements due to decreased atmospheric attenuation and turbulence losses. Specifically, a budget improvement for the 2 and 3 Tundra satellite constellations respectively, for uplinks: 4.1 dBm and 4.7 dBm, and downlinks: 2.9 dBm and 3.5 dBm. This translates to a substantial gain in data rate for Binary Phase Shift Keying (BPSK) modulation at e-9 BER:

- GEO - 122 Gb/s uplink & 21 Gb/s downlink
- Tundra 2 satellite constellation - 313 Gb/s uplink & 45 Gb/s downlink
- Tundra 3 satellite constellation - 359 Gb/s uplink & 54 Gb/s downlink

For high availability services, assessing the required link-margin for operation during 99% confidence turbulence conditions reveals that GEO links degrade significantly. Requiring substantial additional margins of 11.5 dB for uplink and 7.8 dB for downlink. Tundra constellation, benefiting from high link elevation, require a smaller margin 7 dB and 6.3 dB at most for two and three satellites arrays. In 99% strong turbulence conditions the unmitigated link performance from and to Esquimalt would be:

- GEO - 9 Gb/s uplink & 2 Gb/s downlink
- Tundra 2 satellite constellation - 68 Gb/s uplink & 12 Gb/s downlink
- Tundra 3 satellite constellation - 79 Gb/s uplink & 14 Gb/s downlink

Taking into account anisoplanatism losses in the current configuration, a two satellite Tundra constellation would give a factor 2.56x increase in mean uplink data rate, and three satellite array a factor 2.94x. Operating under 99% turbulence conditions would necessitate a considerable increase in the number of transmission apertures. Taking 47 and 30 dBm as reasonable limits to set on transmitted optical power. For Tundra two and three this would respectively require 15 and 13 apertures to achieve 1 Tb/s throughput, which could be spread over 2 or 3 pointing assemblies to minimise throughput loss during handovers. Operation of a 1 Tb/s uplink to GEO with a projected data rate of 9 Gb/s for a single aperture would on the other hand lead to unrealistically large ground-segments.

Alternatively to maintain continuous operations, one could consider increasing availability with additional site diversity, introducing coupled low-turbulence and cloud-free line-of-sight statistics. To illustrate this effect the cloud-free line-of-sight availability of the Canadian OGS network [61] has been revisited. Adjusting the individual OGS probabilities to reflect a loss of 17% availability with no link margin and 1% with margin for turbulence. The initial 92.16% availability of this 8 OGS network would then decrease to 87.14% or 91.92% without and with turbulence margin.

The the large projected impact of anisoplanatism losses for this 20 cm aperture uplink tip-tilt corrected configuration is notable. Which for the high elevation Tundra concepts corresponds to a 1.2 dB to 2.5 dB loss, while for GEO it amounts to 2.6 to 5 dB, for HV57 and HV* respectively. This is a considerable impact on the link budget. If these losses would not be accounted for in the link budget analysis the uplink data rates would increase to 221, 28 Gb/s for GEO, Tundra-2 358, 103 Gb/s and 451, 130 Gb/s Tundra-3, for HV57 and HV* respectively.

The link budget analysis presented here for a ground station located in Esquimalt, Victoria Canada illustrates the comparative performance of the proposed Tundra constellation with respect to GEO. Significant improvements of the mean data rate justify the additional investment in launches and satellites from a $/bit perspective. Furthermore, requiring considerable smaller link margins to ensure operations in stronger turbulence scenario. Allowing for the not only a reduction in size of the required OGS but also that of the OGS network to provide continuous availability.

TABLE VII: Tundra 2 - mean link budget to Esquimalt, handover/apoapsis

Parameter	Uplink	Downlink
Link length (km)	44213/48863	44213/48863
Elevation angle (deg)	55.2/67.7	55.2/67.7
Point ahead angle (μrad)	18.2/15.1	0
Tx beamwaist (cm)	7.1	8.8
Tx power (dBm)	47	30
Tx antenna gain (dB)	112.2	114.1
Tx optical loss (dB)	-3.0	-3.0
Tx jitter pointing loss (dB)	-1.6	-2.5
Free-space loss (dB)	-290.7/-291.2	-290.7/-291.2
Absorption loss (dB)	-0.53/-0.49	-0.53/-0.49
Scintillation p<0.01 (dB)	-3.2/-3.0	-2.3/-1.9
Mean Strehl (dB)	-0.8/-0.7	-1.2/-1.0
Mean anisoplanatism loss (dB)	-0.5/-0.3	0
Scintillation ani. p<0.01 (dB)	-0.7/-0.5	0
Rx diameter (cm)	25	50
Rx antenna gain (dB)	114.1	120.1
Rx optical loss (dB)	-3	-3
Total Rx power (dBm)	-30.7/-31.3	-38.9/-39.7
Link margin (dB)	3	3
Target BER ()	e-9	e-9
Ideal data rate BPSK (Gbs)	359/313	54/45

TABLE IX: Tundra 3 - mean link budget to Esquimalt, handover/apoapsis

Parameter	Uplink	Downlink
Link length (km)	44213/44662	44213/44662
Elevation angle (deg)	65.2/66.9	65.2/66.9
Point ahead angle (μrad)	17.9/16.7	0
Tx beamwaist (cm)	7.1	8.8
Tx power (dBm)	47	30
Tx antenna gain (dB)	112.2	114.1
Tx optical loss (dB)	-3.0	-3.0
Tx jitter pointing loss (dB)	-1.6	-2.5
Free-space loss (dB)	-291.1/-291.2	-291.1/-291.2
Absorption loss (dB)	-0.50/-0.49	-0.50/-0.49
Scintillation p<0.01 (dB)	-3.0/-3.0	-2.0/2.0
Mean Strehl (dB)	-0.7/-0.7	-1.0/-1.0
Mean anisoplanatism loss (dB)	-0.4/-0.4	0
Scintillation ani. p<0.01 (dB)	-0.6/-0.6	0
Rx diameter (cm)	25	50
Rx antenna gain (dB)	114.1	120.2
Rx optical loss (dB)	-3	-3
Total Rx power (dBm)	-30.7/-30.7	-38.9/-38.9
Link margin (dB)	3	3
Target BER ()	e-9	e-9
Ideal data rate (Gbs)	359	54/54

TABLE VIII: Tundra 2 - 99% turbulence link margin to Esquimalt, handover/apoapsis

Parameter	Uplink	Downlink
Scintillation p<0.01 (dB)	-5.5/-5.0	-4.3/-3.9
Mean Strehl (dB)	-2.3/-2.0	-3.4/-2.9
Mean anisoplanatism loss (dB)	-1.0/-0.7	0
Scintillation ani. p<0.01 (dB)	-1.5/-1.1	0
Unmitigated data rate (Gbs)	70/68	13/12
Required margin w.r.t. mean (dB)	7.1/6.6	6.3/-5.6

TABLE X: Tundra 3 - 99% turbulence link margin to Esquimalt, handover/apoapsis

Parameter	Uplink	Downlink
Scintillation p<0.01 (dB)	-5.2/-5.1	-4.0/-3.9
Mean Strehl (dB)	-2.1/-2.0	-3.0/-2.9
Mean anisoplanatism loss (dB)	-0.9/-0.8	0
Scintillation ani. p<0.01 (dB)	-1.3/-1.2	0
Unmitigated data rate (Gbs)	79/86	14/15
Required margin w.r.t. mean (dB)	6.6/6.2	5.8/5.7

VII. Conclusions

In this study, we have conducted a comprehensive analysis comparing the performance of Tundra satellite constellations with a traditional Geostationary orbit configuration for the coverage of high latitude regions. With a general examination of orbital characteristics and detailed analysis of anisoplanatism and overall link budget performance.

Our investigation of anisoplanatism effects on mean and scintillation losses for tip-tilt corrected uplink budgets, revealed substantial link budget impacts. For the low elevation GEO configuration, losses ranged from -2.6 to -5 dB. In contrast, links to Tundra with elevation angles beyond 50 deg would experience considerably lower losses, although still significant from -1.2 to -2.5 dB. These findings highlight the compounded atmospheric losses at low elevation angles and underscore the necessity of accounting for these factors in future satellite system studies.

Feasibility concerns of Tundra orbits have been addressed showing that for low-to-moderate eccentricity Tundra orbits exhibit lower accumulated radiation dosages,and comparable charging environments. Orbit insertion, end-of-life and station keeping cost have furthermore been proven to be as-good-as or better than GEO.

A case study focusing on very high throughput satellites using a domestic optical ground station network in Canada was conducted. Tundra orbits for both two and three satellite configurations have been optimised to maximize optical feeder link performance, selecting a two satellite system with an eccentricity of 0.3 and inclination of 63.4 deg, and a three satellite system with an eccentricity of 0.2 and inclination of 63.4 deg.

Our link budget analysis indicated that Tundra orbits significantly enhance mean data rates under HV57 conditions, offering increases of 2.56x and 2.94x compared to GEO for two and three satellite constellations respectively. Furthermore, while GEO operations in 99% probability turbulence conditions would require significant additional link margins (11.5 dB for uplink and 7.8 dB for downlink), leading to an unrealistic expansion of the ground segment. Tundra constellations could maintain operations with a margin of 7 dB on the uplink and 6.3 dB on the downlink. This means a lay-out of 15 and 13 Tx apertures of 20 cm diameter could achieve a cumulative 1 Tb/s uplink under 90% of turbulence condition, for two and three satellite configuration respectively. Suggesting that as small Tundra constellations could remain operational under more challenging atmospheric conditions, whereas GEO would need to make use of diversity techniques necessitating the expansion of the OGS network, or reducing network availability with up to 6.02 percent points.

Overall, this study highlights the significant advantages of Tundra satellite constellations over a traditional GEO architecture for high-latitude services. Highlighting the impact of link

elevation angle on optical link performance and how system design should adapt.

References

[1] Hemani Kaushal and Georges Kaddoum. "Optical Communication in Space: Challenges and Mitigation Techniques". In: *IEEE Communications Surveys & Tutorials* 19.1 (2017), pp. 57–96. DOI: 10.1109/COMST.2016.2603518.

[2] Vardan Semerjyan et al. "Optical feeder links for GEO satellites at Viasat Inc." In: *Free-Space Laser Communications XXXVI*. Vol. 12877. SPIE. 2024, pp. 510–521.

[3] Sylvain Poulenard, Michael Crosnier, and Angélique Rissons. "Ground Segment Design for Broadband Geostationary Satellite With Optical Feeder Link". In: *Journal of Optical Communications and Networking* 7.4 (2015), pp. 325–335.

[4] Amar Mody and Eva Gonzalez. "An operator's view: The medium-term feasibility of an optical feeder link for VHTS". In: *2017 IEEE International Conference on Space Optical Systems and Applications (ICSOS)*. IEEE. 2017, pp. 278–285.

[5] Airbus Defence and Space. *Next steps in optical communication in space*. ESA EPIC Meeting on New Space 2019. Sept. 2019.

[6] Dirk Giggenbach et al. "A high-throughput satellite system for serving whole europe with fast internet service, employing optical feeder links". In: *Broadband Coverage in Germany. 9th ITG Symposium. Proceedings*. VDE. 2015, pp. 1–7.

[7] Nicolas Perlot et al. "Optical GEO feeder link design". In: *2012 Future Network & Mobile Summit (FutureNetw)*. IEEE. 2012, pp. 1–8.

[8] Bischl H. et al. *Feasibility Assessment of Optical Technologies and Techniques for Reliable High Capacity Feeder Links*. Tech. rep. ESA, 2010.

[9] *High Throughpit Optical Network Demonstration System (HYDRON-DS) - Thematic Call Guidelines*. Tech. rep. ESA, 2023.

[10] Vardan Semerjyan et al. "Optical feeder links for GEO satellites at Viasat Inc." In: *Free-Space Laser Communications XXXVI*. Vol. 12877. SPIE. 2024, pp. 510–521.

[11] Dirk Giggenbach and Amita Shrestha. "Atmospheric absorption and scattering impact on optical satellite-ground links". In: *International Journal of Satellite Communications and Networking* 40.2 (2022), pp. 157–176.

[12] Hamid Hemmati. *Near-earth laser communications*. Vol. 1. CRC press, 2020.

[13] Renny Fields et al. "5.625 Gbps bidirectional laser communications measurements between the NFIRE satellite and an optical ground station". In: *2011 International Conference on Space Optical Systems and Applications (ICSOS)*. IEEE. 2011, pp. 44–53.

[14] Larry B Stotts and Larry C Andrews. "Optical communications in turbulence: a tutorial". In: *Optical Engineering* 63.4 (2024), pp. 041207–041207.

[15] F. Kneizys et al. "User guide to LOWTRAN 7". In: (Aug. 1988), p. 146.

[16] Meg Noah. *LOWTRAN7 Aerosol Models and Atmosphere Profile Data*. MATLAB Central File Exchange, 22 April 2019 https://www.mathworks.com/matlabcentral/fileexchange/71018-lowtran7-aerosol-models-and-atmosphere-profile-data. Accessed: 12 April 2024.

[17] Michael Hirsch. *lowtran 3.1.0*. Pypi, February 2023 https://pypi.org/project/lowtran/3.1.0/. Accessed: 12 April 2024.

[18] Dirk Giggenbach. "Optimierung der optischen freiraumkommunikation durch die turbulente atmosphäre-focal array receiver". PhD thesis. Shaker-Verlag, 2005.

[19] David L Fried. "Anisoplanatism in adaptive optics". In: *JOSA* 72.1 (1982), pp. 52–61.

[20] Hemani Kaushal, V.K. Jain, and Subrat Kar. *Free Space Optical Communication*. Springer, 2017. ISBN: 1935-3839.

[21] Thang V Nguyen et al. "Link availability of satellite-based FSO communications in the presence of clouds and turbulence". In: *IEICE Communications Express* 10.5 (2021), pp. 206–211.

[22] Donald L Walters and L William Bradford. "Measurements of r 0 and θ 0: two decades and 18 sites". In: *Applied optics* 36.30 (1997), pp. 7876–7886.

[23] DL Walters, DL Favier, and JR Hines. "Vertical path atmospheric MTF measurements". In: *JOSA* 69.6 (1979), pp. 828–837.

[24] Randall J Alliss and Billy D Felton. "Quantifying Atmospheric Impacts on Space Optical Imaging and Communications". In: *Advanced Maui Optical and Space Surveillance Technologies Conference*. 2011, E43.

[25] Héctor Vázquez Ramió et al. "European extremely large telescope site characterization. II. High angular resolution parameters". In: *Publications of the Astronomical Society of the Pacific* 124.918 (2012), p. 868.

[26] FD Eaton et al. "Isoplanatic angle direct measurements and associated atmospheric conditions". In: *Applied optics* 24.19 (1985), pp. 3264–3273.

[27] Robert J Noll. "Zernike polynomials and atmospheric turbulence". In: *JOsA* 66.3 (1976), pp. 207–211.

[28] Yukun Wang et al. "Performance analysis of an adaptive optics system for free-space optics communication through atmospheric turbulence". In: *Scientific reports* 8.1 (2018), p. 1124.

[29] Klaus Kudielka et al. "Optical feeder link demonstrations between the ESA Optical Ground Station and Alphasat". In: *2023 IEEE International Conference on Space Optical Systems and Applications (ICSOS)*. IEEE. 2023, pp. 64–68.

[30] Hongtao Zhang et al. “Low-order mode correction anisoplanatism limitations for adaptive optics system”. In: *Optical Engineering* 42.8 (2003), pp. 2190–2196.

[31] Richard J Sasiela. *Electromagnetic wave propagation in turbulence: evaluation and application of Mellin transforms*. Vol. 18. Springer Science & Business Media, 2012.

[32] Ronald Parenti et al. “Modeling the PDF for the irradiance of an uplink beam in the presence of beam wander”. In: *Atmospheric Propagation III*. Vol. 6215. SPIE. 2006, pp. 42–54.

[33] Larry C Andrews et al. “Beam wander effects on the scintillation index of a focused beam”. In: *Atmospheric Propagation II*. Vol. 5793. SPIE. 2005, pp. 28–37.

[34] Larry C Andrews and Ronald L Phillips. “Laser beam propagation through random media”. In: *Laser Beam Propagation Through Random Media: Second Edition* (2005).

[35] Larry C Andrews et al. “Strehl ratio and scintillation theory for uplink Gaussian-beam waves: beam wander effects”. In: *Optical Engineering* 45.7 (2006), pp. 076001–076001.

[36] Larry C Andrews, Ronald L Phillips, and Cynthia Y Hopen. *Laser beam scintillation with applications*. Vol. 99. SPIE press, 2001.

[37] Scot S Olivier and Donald T Gavel. “Tip–tilt compensation for astronomical imaging”. In: *JOSA A* 11.1 (1994), pp. 368–378.

[38] D Alaluf and JM Perdigues Armengol. “Ground-to-satellite optical links: how effective is an uplink Tip/Tilt pre-compensation based on the satellite signal?” In: *CEAS Space Journal* (2021), pp. 1–12.

[39] George C Valley. “Isoplanatic degradation of tilt correction and short-term imaging systems”. In: *Applied Optics* 19.4 (1980), pp. 574–577.

[40] T Sean Ross. “Limitations and applicability of the Maréchal approximation”. In: *Applied optics* 48.10 (2009), pp. 1812–1818.

[41] Paul D Shubert. “Anisoplanatic effects in moderate aperture laser communication system uplinks”. In: *Free-Space Laser Communications XXXI*. Vol. 10910. SPIE. 2019, pp. 348–355.

[42] Stefano DiPierro, Riza Akturan, and Richard Michalski. “Sirius XM Satellite Radio system overview and services”. In: *2010 5th Advanced Satellite Multimedia Systems Conference and the 11th Signal Processing for Space Communications Workshop*. IEEE. 2010, pp. 506–511.

[43] Yuri Ulybyshev. “Satellite constellation design for continuous coverage: short historical survey, current status and new solutions”. In: *Proceedings of Moscow Aviation Institute* 13.34 (2009), pp. 1–25.

[44] David A Vallado. *Fundamentals of astrodynamics and applications*. Vol. 12. Springer Science & Business Media, 2001.

[45] Victor U J Nwankwo, Nnamdi N Jibiri, and Michael T Kio. “The impact of space radiation environment on satellites operation in near-Earth space”. In: *Satellites Missions and Technologies for Geosciences* (2020), pp. 73–90.

[46] HC Koons et al. “The impact of the space environment on space systems”. In: *NASA STI/Recon Technical Report N* (1999), pp. 69036–69041.

[47] D Heynderickx et al. “New radiation environment and effects models in the European Space Agency’s Space Environment Information System (SPENVIS)”. In: *Space Weather* 2.10 (2004).

[48] Larisa D Trichtchenko et al. “Highly elliptical orbits for arctic observations: Assessment of ionizing radiation”. In: *Advances in Space Research* 54.11 (2014), pp. 2398–2414.

[49] TP O’Brien et al. “Changes in ae9/ap9-irene version 1.5”. In: *IEEE Transactions on Nuclear Science* 65.1 (2017), pp. 462–466.

[50] Michael Anthony Xapsos et al. *Space environment effects: Model for emission of solar protons (ESP): Cumulative and worst case event fluences*. Tech. rep. 1999.

[51] MA Xapsos et al. “Model for cumulative solar heavy ion energy and linear energy transfer spectra”. In: *IEEE Transactions on Nuclear Science* 54.6 (2007), pp. 1985–1989.

[52] Allan J Tylka et al. “CREME96: A revision of the cosmic ray effects on micro-electronics code”. In: *IEEE Transactions on Nuclear Science* 44.6 (1997), pp. 2150–2160.

[53] Stephen M Seltzer. “Updated calculations for routine space-shielding radiation dose estimates: SHIELDOSE-2”. In: (1994).

[54] Wayan Suparta and Siti Katrina Zulkeple. “Spatial analysis of galactic cosmic ray particles in low earth orbit/near equator orbit using SPENVIS”. In: *Journal of Physics: Conference Series*. Vol. 495. 1. IOP Publishing. 2014, p. 012040.

[55] Joseph F Fennell et al. “Internal charging: A preliminary environmental specification for satellites”. In: *IEEE transactions on plasma science* 28.6 (2000), pp. 2029–2036.

[56] Joseph F Fennell et al. “Spacecraft charging: Observations and relationship to satellite anomalies”. In: *Spacecraft charging technology*. Vol. 476. 2001, p. 279.

[57] Michael J Bruno and Henry J Pernicka. “Tundra constellation design and stationkeeping”. In: *Journal of spacecraft and rockets* 42.5 (2005), pp. 902–912.

[58] Elena Fantino et al. “Geosynchronous inclined orbits for high-latitude communications”. In: *Acta Astronautica* 140 (2017), pp. 570–582.

[59] Alan B Jenkin et al. “Tundra disposal orbit study”. In: *Proceedings of the 7th European Conference on Space Debris, Darmstadt*. 2017.

[60] Alan B Jenkin et al. “Comparison of disposal options for Tundra orbits in terms of delta-V cost and long-term collision risk”. In: *Journal of Space Safety Engineering* 8.1 (2021), pp. 47–62.

[61] Stephane Gagnon et al. “Recent developments in satellite laser communications: Canadian context”. In: *Proceedings of 2012 International Conference on Space Optical Systems and Applications*. 2012, pp. 9–12.

[62] Lynne Genik, Aimee Gunther, and Sylvaijn Raymond. *Canadian RD in Optical and Quantum Communications in Space*. ICSOS 2023. Oct. 2023.

[63] Canadian Radio-television and Telecommunications Commission. *BROADBAND FUND Map of areas that are eligible for funding under the Broadband Fund*. 2023. URL: https://crtc.gc.ca/eng/internet/map-carte.htm (visited on 04/15/2024).

4
Conclusions and Future work

The conducted system study has provided a comprehensive view of the characteristics of Tundra orbits and the potential of optical feederlink implementation for high-latitude regions. A conclusion to the research questions is presented here in addition to an outlook to further developments.

4.1. Conclusions

The answers to the initial research questions are discussed, notably highlighting how the performed research has shifted the focus and importance of different subquestions. Firstly addressing the sub-questions:

1. How does the ground-to-Tundra link architecture affect the optical link budget in an OGS feeder link network?

Ground-to-Tundra link architecture has shown to provide consistent link elevation angle improvements over a large inclination-eccentricity space, providing continuous 50 deg+ elevation coverage to a proposed Canadian OGS network. Link budget analysis for tip-tilt adaptive optics uplinks and aperture averaged downlinks has shown that increased free-space losses due to longer link lengths are more than compensated by the significant reduction of atmospheric attenuation and dynamic turbulence penalties.

Notably, significant losses of mean Strehl due to anisoplanatism have been identified in uplink tip-tilt pre-correction. Further modelling of anisoplanatic induced jitter fade margins has demonstrated an aggregated anisoplanatism effect of up to -5dB, previously unaccounted for in system level studies.

Integrated link budget analysis has shown that, given HV57 turbulence and ideal sky conditions, Tundra orbits provide received uplink power improvements of 4.1 and 4.7 dBm, for a two and three satellite constellations respectively. Which could, respectively result in 2.56x and 2.94x increase of data uplink throughput compared to a GEO link. Not degrading under the added effect of anisoplanatism losses, downlink budgets maintain a significant 2.3 dBm and 3.1 dBm downlink received power improvements for a two and three satellite constellations respectively.

2. What is the optimal constellation and set of orbital parameters in Tundra Orbit for a continuous feeder link connection to an OGS network in Canada?

The optimal orbital parameter set have been restricted and determined following an analysis of the Tundra orbit characteristics. An evaluation of the orbit's ΔV for insertion, end-of-life, and station keeping costs indicates that these parameters generally remain stable throughout the design-space, provided that the orbit is restricted to an inclination of 63.4 degrees to minimize J2 induced argument of perigee rotation.

While overall space environment analysis has shown an improvement for Tundra orbits with respect to GEO. The implementation of highly eccentric orbits (eccentricity greater than 0.3) has been restricted due to concerns over deep charging effects in the outer electron belts.

In this restricted design-space, a set of optimal orbit parameters has been defined by minimising the limiting link losses to the Canadian OGS network of interest. Yielding a two satellite constellation with 0.3 eccentricity, 63.4 inclination, longitude of ascending node of 270/90 deg and mean anomaly of 0/180 deg. A three satellite configuration, which required reduced dwell-time, benefits from lessened

free-space losses with an eccentricity of 0.2, 63.4 inclination, longitude of ascending node of 270/150/30 deg and mean anomaly of 0/120/240 deg.

3. How does the Tundra architecture affect availability statistics for a Canadian OGS network?

Two and three satellite Tundra architectures show increased robustness to strong atmospheric turbulence conditions. Requiring link budget margins of 3-4.5 dB less than a GEO link to operate under 99% confidence turbulence conditions. Sizing of a ground segment to operate for 99% margin gives a reasonable ground segment 13 to 15 Tx aperture for Tb/s uplink to the two Tundra constellation. By contrast the GEO ground-segment would grow to unfeasible proportions for 99% conditions operations, necessitating additional OGS site diversity to mitigate turbulence conditions.

The projected impact on availability, with GEO restricted to operating under 83% HV57 conditions, results in a 6.02 percent points reduction of availability in a Canadian OGS network. Tundra links having been shown to be feasible under 99% turbulence conditions would result in minor 0.14 percent point loss of OGS network availability.

4. To what extent is the implementation of Tundra feeder links competitive to proposed GEO designs?

Feasibility concerns have been addressed showing that for low-to-moderate eccentricity Tundra orbits exhibit lower accumulated radiation dosages and comparable charging environments. Orbit insertion, end-of-life and station keeping cost have furthermore been proven to be as-good-as or better than GEO. Link budget analysis furthermore suggest considerable data rate and availability improvements following reduced atmospheric propagation paths.

These benefits are offset by a two to threefold increase in space-segment expenditure for Tundra satellite constellation configurations. Yet, the increased mean uplink data rate of 2.56x for two satellites and 2.94x for three suggests a cost-per-bit advantage for the two-satellite configuration, achieving nearly break-even for the three-satellite setup. Additionally, the reduced link budget margins for strong turbulence conditions present opportunities for decreasing OGS on-site redundancy or reducing required OGS site diversity.

With specific aspects and findings of this study addressed by the sub-research question, a general synthesis of this thesis can be given through the answer to the main research question:

To what extent could a Very-High Throughput Satellite constellation in Tundra improve space-ground optical feeder link throughput and availability in Canada when compared to the GEO architecture?

Overall, the study underscores the potential of small Tundra constellations to enhance satellite communication infrastructure, with a more efficient and robust service in a region where GEO faces limitations. Feasibility concerns related to the radiation environment have been addressed and show net improvements for many Tundra orbits. General orbit characteristics have been shown to produce comparable ΔV cost but do highlight room for optimisation and further analysis on orbit control. Link budget analysis have been used to show consistent improvements observed in average conditions which extend further to scenarios involving strong turbulence and atmospheric attenuation.

4.2. Recommendation and future work

The results of this study can be used to derive general implications and recommendations for further work. These have been summarised as follows.

Implications

Centrally, this system study has highlighted the potential of Tundra orbits for optical feeder link applications in high latitude regions. The link budget evaluations demonstrate that Tundra orbits significantly outperform GEO satellites in both average and challenging atmospheric conditions. Resulting in an increase in optical feederlink mean throughput and enhanced robustness to turbulence. With

improvements of such significant margins suggesting that additional investment in a second or third space-segment could be cost effective to GEO. Consequently, this concept merits further analysis on link budget details and implementation aspects. For this, the results can be interpreted as proof of feasibility of Tundra orbits and background, providing a starting point for future detailed analysis.

In addition, the vulnerability of optical links to low-elevation angles has notably been visible in this analysis, where the effects of atmospheric attenuation and dynamic turbulence loss are compounded due to the extended atmospheric propagation path. Highlighting the need to approach orbit coverage analysis for optical links as a function of elevation angle. The approach of limiting link coverage has proven effective for the evaluation of conservatively budgeted availability continuous services.

Furthermore, the analysis has revealed that the implementation of mean Strehl ratios and scintillation fade losses due to anisoplanatism significantly impacts link budget results. This finding highlights a vulnerability in systems characterized by large point-ahead angles, a factor that has received limited attention in optical feeder link demonstrations and system studies. Given its substantial influence on link effectiveness, further experimental research is essential to fully understand this effect. Especially considering faster degradation expected in full AO system with respect to tip-tilt AO. Furthermore, to accurately develop novel systems, it is crucial that the relationship of link geometry and anisoplanatism losses is considered in architecture performance.

Extensive radiation analysis has furthermore shown that, highly inclined a low eccentricity Tundra orbits, experience a more moderate mean radiation and deep charging environments than GEO. However concerns of deep charging arising for orbits with eccentricities beyond 0.2 should be mitigated with additional shielding.

Limitations

The use of analytical modeling for atmospheric turbulence in evaluating dynamic link properties has inherent limitations, though it is deemed sufficient for system-level analysis and is widely implemented as such. A natural next step in the evaluation of Tundra orbits would be numerical optical propagation analysis, trading generality of results for accuracy. Anisoplanatic fade probability has been modeled solely as anisokinetic jitter, leading to an underestimation by excluding higher-order Zernike modes. While an alternative approach is presented in Appendix A it lacks double star validation measurements as is the case for the current implementation. Future improvement would include the current anisoplanatism modelling approach to be integrated in a unified scintillation fade probability distribution. Which in addition, would be a good development to stimulate the adoption of anisoplanatism budgeting is system studies.

This study utilized statistics of r_0, θ_0 and cloud-free-line-of-sight probabilities to analysis link availability, not considering potential correlations and typical diurnal variations. As a result, the availability figures in practice could fall short. In the future, combined atmospheric cloud, attenuation and turbulence datasets through studies like ESA's Anatolia project will be crucial in incorporating these effects. Additionally, availability figures presented have been based on a proposed OGS network in Canada, which must be expanded considerably to provide true 99.9% Furthermore, requiring modelling improvements to correlation between OGS sites.

Current estimates of orbit control costs are based on generalized perturbations; future work could refine these estimates by detailing the perturbation for each individual satellite through numerical long-term propagation.

Opportunities

As a system study the opportunity of future research are quite endless, either going more into detail or spreading broad and considering new aspects. The points below have been identified as the most relevant to the analysis in this thesis.

Further refinement of channel properties could include expanding link fade analysis with fade duration estimates to evaluate link degradation under different coding schemes. Short fades could for example be mitigated to a certain extent by forward error correction and interleaving. Additionally, cloud mitigation could be considered in future studies. Expanding link availability by including a margin for thin cirrus cloud attenuation. Furthermore, sky background radiance would be essential in the future to validate the local time of apogee of Tundra constellations with respect to the Sun. With the link budget configuration based on reference GEO system studies, future analyses could introduce a configuration selection component to determine the optimal setup, such as beam width, for the specific link geometry and environmental conditions.

Future evaluation of Tundra system architectures could first and foremost evaluate perigee pass use cases. Currently only 33% and 50% of the possible payload active time has been analysed, namely during apogee pass. Passes of opportunity or low elevation coverage at the south pole could increase payload usage and further support system competitiveness. A prime opportunity is the retrieval of Earth Observation payload data from polar ground-stations. In this analysis we have shown the possibility to provide OFL compatible coverage to satellite dependent communities. This can be further extend by combining cloud coverage statistics to estimate possible point-to-point transmission throughput. Further optimisation of the Tundra constellation geometry is possible by considering diurnal variation in turbulence and cloud-cover in the phasing of the apogee pass at local time.

Continuing studies on Tundra orbit characteristics could include surface charging estimations and explore the implication on potential reductions in solar panel area due to decreased eclipse duration and Total Ionizing Dose (TID). With the insertion technique considered here being a classical Geostationary Transfer Orbit, future work could investigate novel orbit insertion techniques. Notably Low Earth Orbit insertion followed by electric orbit raising could facilitate the launch of all orbital planes in one launch, utilizing fast natural plane precession at low altitudes to separate the orbital planes. Furthermore the coverage performance evolution of East-West station keeping only strategies could be investigated to reduce ΔV costs.

In conclusion, this initial proof of feasibility has revealed numerous opportunities for further research. Given that optical link performance is central to the potential of this architecture, it is recommended that future research firstly pursues more detailed analysis in this area.

A Link modelling

In the following section the optical link modelling approach is discussed to address in more detail the methodology employed in the scientific paper 'High Throughput Laser Communication to Tundra Orbits'. Discussing model choices, limitations and verification & validation activities.

A.1. Overview

A summary of the link budget components is presented in Table A.1, common and relatively simple equations are directly given here. Contributions which require some extra discussion are referred to their relevant section.

Parameter	Description	Definition	Reference
	Static budget contributions		
P_{TX}	Transmitter power (dBm)	subsection A.1.1	
G_{TX}	Transmitter gain (dB)	$10log\left[\frac{8}{\theta_{div}^2}\right]$	[18, chapter 7]
L_{TX}	Transmitter efficiency loss (dB)	subsection A.1.1	
G_{RX}	Receiver gain (dB)	$10log\left[(\frac{2\pi \cdot r_{rx}}{\lambda})^2\right]$	ITU-R S.1590
L_{RX}	Receiver efficency loss (dB)	subsection A.1.1	
L_{ATM}	Atmospheric attenuation loss (dB)	subsection A.1.2	
L_{pe}	Pointing offset loss (dB)	$10log\left[e^{-2\theta_\epsilon^2/\theta_{div}^2}\right]$	[18, chapter 7]
L_{FSL}	Free space loss (dB)	$10log\left[(\frac{\lambda}{4\pi R})^2\right]$	ITU-R S.1590
	Dynamic budget contributions		
L_{Strehl}	Mean Strehl loss (dB)	subsection A.2.2	
$L_{fade\ sci}$	Scintillation fade margin (dB)	subsection A.2.3	
$L_{Strehl\ ani}$	Mean anisoplanatism Strehl loss (dB)	subsection A.2.4	
$L_{fade\ sci\ ani}$	Anisokinetic jitter fade margin (dB)	subsection A.2.4, chapter 3	
L_{pj}	Pointing jitter loss (dB)	$10log\left[e^{-4\sigma_\epsilon^2/\theta_{div}^2}\right]$	[18, chapter 2]
	Budget		
$P_{RX} = P_{TX} + G_{TX} + L_{TX} + G_{RX} + L_{RX} + L_{ATM} + L_{pe}$ $+L_{fade\ sci} + L_{Strehl} + L_{Strehl\ ani} + L_{fade\ sci\ ani} + L_{pj}$			

Table A.1: Link budget overview

A.1.1. Link budget inputs

In order to provide a link budget configuration representative for VHTS a review of relevant system studies addressing optical feederlink performance to GEO was performed. This is done to provide a link budget analysis which can be directly compared to existing literature.

Notably BATS [19] has been taken as a reference to determine the configuration as:

- TX OGS: 20cm aperture, 47dBm power, optical efficiency loss -3dB
- RX OGS: 50cm aperture, optical efficiency loss -3 dB
- TX VHTS: 25cm aperture, 30dBm power, optical efficiency loss -3dB
- RX VHTS: 50cm aperture, optical efficiency loss -3dB

With tip-tilt pre-correction adaptive optics on the uplink TX and aperture averaging on the downlink RX.

The detector configuration has furthermore been assumed as a coherent homodyne detector with Binary Phase Shift Keying (BPSK) modulation. Yielding a sensitivity of average 9 photons per bit at 10^{-9} BER. This gives, for 1 Gb/s at 1.55μm a required average RX power of -59.3 dBm [12], varying with with data rate following,

$$P_{RX} = n_{photons} B \frac{hc}{\lambda}, \tag{A.1}$$

with $n_{photons}$ the average number of photons, B the data rate, h the Planck constant and c the speed of light.

A notable limitation in this approach is the lack of optimisation of the TX and RX configuration for environmental conditions. Furthermore data rate is presented as a theoretical limit, not accounting for increased inefficiencies in hardware for high data rates or background noise contributions.

A.1.2. Atmospheric attenuation

The LOWTRAN 7 model [20] was employed to estimate atmospheric transmittance under various atmospheric conditions. This model, originally written in Fortran, has been accessed through the wrappers for aerosol [21] and molecular [22] attenuation.

In these simulations the line by line molecular and aerosol (background and volcanic) atmospheric composition of the atmosphere is taken. With each atmospheric constituent defined by wavelength dependent absorption and scattering properties, providing an aggregated attenuation coefficient γ along the line-of-sight [18, chapter 2]:

$$\gamma(\lambda) = \underbrace{\alpha_m(\lambda)}_{\text{Molecular absorption}} + \underbrace{\alpha_a(\lambda)}_{\text{Aerosol absorption}} + \underbrace{\beta_m(\lambda)}_{\text{Molecular scattering}} + \underbrace{\beta_a(\lambda)}_{\text{Aerosol scattering}} \tag{A.2}$$

Which is integrated over the atmospheric propagation path to determine cumulative loss as follows,

$$L_{att} = 10log\left(e^{-\int_{L_0}^{L_1} \gamma(z)\delta z}\right) \tag{A.3}$$

A.1.3. Verification and Validation strategy

Link budget verification has been performed at two levels:

- Module-level - Unit test for the verification of correct implementation of different models, implemented as automated numerical assertion tests or via the reproduction of figures of reference papers. To maintain report readability unit test results are not discussed, with the exception of adapted and newly developed models.
- (Link) Model-level - Integrated test for the verification of the correct link budget results. Reproduced optical link budgets of Orelia [12] and BATS [**roy2015optical.**]

A.2. Dynamic link budget

The following section will provide some additional background on the modelling of the propagation of waves through atmospheric turbulence. Firstly, introducing the fundamental principles and assumptions. Followed by background on mean Strehl model, scintillation estimation and anisoplanatism are discussed. Including a comparison to other models considered and V&V activities.

A.2.1. Principles

The estimation of the impact of these small scale fluctuations on optical communication is based on the statistical moments of the optical field $U(\vec{r}, L)$ governed by the reduced wave equation with a varying refractive index n,

$$\nabla^2 U(\vec{r}) + k^2 n\vec{r}^2 U\vec{r} = 0. \tag{A.4}$$

assuming that,

- wave back scattering can be neglected
- wave depolarization effects can be neglected
- refractive index gradient is correlated in the direction of propagation
- the parabolic (paraxial) approximation can be invoked

Although, the above equation already takes quite some simplifications into account it is complex to solve. Based on the Rytov approximation for weak perturbation a perturbed electrical field can be expressed as

$$U(\vec{r}, L) = U_0(\vec{r}, L)e^{\Phi_1(\vec{r},L)+\Phi_2(\vec{r},L)+\ldots} \tag{A.5}$$

where Φ represents the series of complex phase perturbations induced by the propagation medium. Through detailed derivation using the Rytov approximation, first-order moments such as the phase variance can be determined. According to Sasiela [23, chapter 2], the phase variance is given by:

$$\sigma_\phi^2 = 0.2073k_0^2 \int_0^L C_n^2(z)dz \int_0^\infty f(\kappa)cos^2[P(\gamma, \kappa, z)]F(\gamma, \vec{\kappa})d\vec{\kappa} \tag{A.6}$$

in which k_0 is the wave number, $P(\gamma, \kappa, z)$ the diffraction parameter and$F(\gamma, \vec{\kappa})$ a filter functions. These filter functions are a central aspect of the analysis of turbulence statistics, enabling the extraction of the amplitude and phase statistics of specific Zernicke modes. This ability has been used to derive scintillation and mean Strehl loss implementations described in this appendix.

Furthermore, $f(\kappa)$ represents the turbulence spectrum, describing the distribution of energy in the medium for different wave numbers κ. In following analysis the Kolmogorov spectrum is taken, describing the inertial flow down of energy by the power -5/3. As illustrated in Figure A.1 the inner and outer range define the end of the spectrum for respectively small and large turbulent eddy's. While generally implemented for its simplicity, other representations such as Hill or the Modified Atmospheric Spectrum are considered more accurate [24]. We do however, chose to adhere to this model throughout our analysis to maintain generality and for ease of derivation.

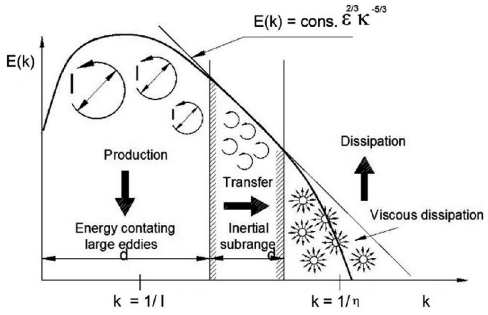

Figure A.1: Kolmogorov representation of turbulence [25]

A.2.2. Strehl ratio

The Strehl ratio provides a metric to define the ratio of the perturbed focused beam to that of a ideal beam. Ideally the projected beam would be represented as an Airy disk however, offsets over the wavefront would lead to losses in imaged power. These losses are computed from the phase variance over the wavefront at the receiver aperture using the extended Maréchal approximation:

$$S \approx= e^{-\sigma_\phi^2} \tag{A.7}$$

Through the determination of the Strehl ratio the mean expected loss due to turbulence induced phase variance can be determined. The derivation of the implemented phase variance expression can be found in chapter 3, the result is repeated here as:

$$\sigma_{\phi\ fig}^2 = 0.546\pi k_0^2 \int_0^L C_n^2(z)dz \int \kappa^{-8/3} \left(1 - \left[\frac{2J_1(\gamma\kappa D/2)}{\gamma\kappa D/2}\right]^2 - \left[\frac{4J_2(\gamma\kappa D/2)}{\gamma\kappa D/2}\right]^2\right) d\vec{\kappa},$$

for tip-tilt corrected beams and Kolmogorov turbulence spectrum.

Comparison

To verify the implementation of this tip-tilt corrected phase variance it is here compared to several other accepted methods, all following from implementation of the extended Maréchal approximation. Firstly, from Noll [26] gives tip tilt removed phase variance as:

$$[\sigma_\phi^2]_{fig} \approx 0.134(D/r_0)^{5/3} \tag{A.8}$$

, which should agree with the derivation of chapter 3 through Sasiela for HV57 C_n^2. Andrews [27] is also considered here without tip-tilt correction,

$$SR_{fig} \approx \frac{1}{1 + (D/r_0)^{5/3}},\ D/r0 < 1 \tag{A.9}$$

and adapted to incorporate tip-tilt correction [28]:

$$SR_{fig} \approx= \left[1 + \left(5.56 - \frac{4.84}{1 + 0.04(w_0/r_0)^{5/3}}\right)(w_0/r_0)^{5/3}\right]^{-6/5} \tag{A.10}$$

These implementations are presented in Figure A.2. The effect of tip-tilt adaptive optics correction is evident from these models with Andrews without tip-tilt correction showing notable lower Strehl ratio compared to tip-tilt corrected cases. An expected results as indeed wavefront tilt at the receiving aperture induces a degradation in the focused beam. Furthermore our expression of phase variance shows good agreement with the other tip-tilt corrected approaches.

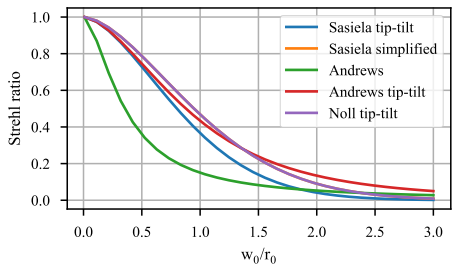

Figure A.2: Strehl ratio model comparison

A.2.3. Scintillation fades

Scintillation refers to rapid fluctuations in received signal intensity at the receiver caused by destructive and constructive interference during propagation. Scintillation is determined analytically by using the second-order moment evaluation of the mutual coherence function at two identical points. Stemming

from the Rytov solution to the perturbed wave-equation methods have been developed to expand its validity beyond weak turbulence conditions. The implementation of these models will be discussed here, together with a comparison and V&V.

Characterisation of the scintillation effects in an optical link follows from the definition of the scintillation index from the irradiance I,

$$\sigma_I = \frac{\langle I^2 \rangle}{\langle I \rangle^2} - 1 \tag{A.11}$$

a measure of signal intensity variation implemented through appropriate probability density functions to determine key signal characteristics. The implication of turbulence on signal intensity is considered separately for uplink and downlink beam. With uplink beams notably suffering from beamwander effects and downlink beam making use of aperture averaging.

Uplink beam

We implement Andrews' model for strong turbulence which treats the diverging uplink beam as a spherical point sources, with Rytov variance defined as,

$$\sigma_R^2 = 2.25\mu_3 k^{7/6}(H - h_0)^{5/6} sec(\xi)^{11/6} \tag{A.12}$$

where the third moment of turbulence is,

$$\mu_3 = \int_{h_0}^{H} C_n^2(h)\xi^{5/6}(1-\xi)^{5/6} dh \tag{A.13}$$

and $\xi = 1 - (h - h_0)/(H - h_0)$. This expression of the Rytov variance can be used in weak fluctuation regimes, however would lose validity under strong turbulence and as such also for large zenith angles. Andrews extends this method to the strong perturbations regime, by separating small-scale and large-scale log-irradiance variance through spatial filter functions on the Kolmogorov spectrum. These act as high-pass and low pass filter for turbulence spectrum, the complete derivation is not included here and can be consulted in Andrews et al. [10], resulting in the scintillation index for weak to strong turbulence:

$$\sigma_I^2 = exp\left[\frac{0.49\sigma_R^2}{\left(1 + 0.56\sigma_R^{12/5}\right)^{7/6}} + \frac{0.51\sigma_R^2}{\left(1 + 0.69\sigma_R^{12/5}\right)^{5/6}}\right] - 1 \tag{A.14}$$

In addition, the scintillation estimation method proposed by Parenti [29] is considered. This also extends the applicability of the Rytov theory to strong turbulence regimes. Furthermore, this model includes a statistical model of the induced beamwander losses. As a propagating optical beam will experience large-scale deflections, causing short term skewed beam profiles at the receiver. Firstly the Rayleigh range is used to define the definition of near-field and far-field turbulence effect, corresponding to the point at which a Gaussian beams cross-section has been doubled:

$$z_R = \frac{kw_0^2}{2}\left[1 + \frac{kw_0^2}{2L}\right]^{-1} \tag{A.15}$$

The far field turbulence follow similarly as in Andrews from the Rytov variance,

$$\left[\sigma_I^2\right]_{FF} = 2.25k^{7/6}\int_{z_R}^{L} C_n^2(z) z^{5/6}\left(\frac{L-z}{L}\right)^{5/6} dz \tag{A.16}$$

note here the notation difference indicating propagation path z as integration parameter instead of altitude h. Then the fried parameter of the near-field turbulence as,

$$r_{0\ ap} = \left[0.423k^2\int_0^{z_R} C_n^2(z)\left(\frac{L-z}{L}\right)^{5/3} dz\right]^{-3/5} \tag{A.17}$$

The near-field tilt effects are applied as a Gaussian tilt jitter in a Strehl distribution. For a non tip-tilt corrected beam this gives,

$$\left[\sigma_I^2\right]_{NF} = \left[0.77(w_0/r_{0\ ap})^{-5/3} + exp\left(-5(w_0/r_{0\ ap})^{-5/3}\right)\right]^{-1} \tag{A.18}$$

Where the second term is a heuristic correction, which accounts for the increase in scintillation observerd in numerical propagation at $w_0/r_0 = 2$. Accounting for tip-tilt correction mitigating beam wander the near-field turbulence effect is given as,

$$\left[\sigma_I^2\right]_{NF,\ fig} = \left[10.9(w_0/r_{0\ ap})^{-11/6} + exp\left(-20(w_0/r_{0\ ap})^{-11/6}\right)\right]^{-1} \tag{A.19}$$

with again a heuristic correction for an overshoot at $w_0/r_0 = 2$. Note the relationship with beamwaist w_0 introduced in the scintillation index with the modelling of beamwander effects, due to the relationship of beam jitter losses and beam waist.

In Figure A.3 the scintillation index of the two models is given for varying ratio w_0/r_0. The area shaded in grey represents the regime in which the link budget analysis has been performed. From this figure it is clear how the ratio of near-field and far-field turbulence effects vary, with almost exclusively near-field effects for $w_0/r_0 < 10^{-1}$ and a drop-off at $w_0/r_0 > 3 \cdot 10^{-1}$. Highlighting the effect beamwander has in the link regime under consideration in this study and showing the limitations of the exclusion of beamwander effects in uplink modelling with significant effects in the region of interest. Consequently the Parenti model including beamwander effects has been used in the study. Figure A.3 provides an additional use of verification of the method by Parenti, which can be compared to another method incorporating beamwander [30], showing very good agreement between these two methods over the entire w_0/r_0 space.

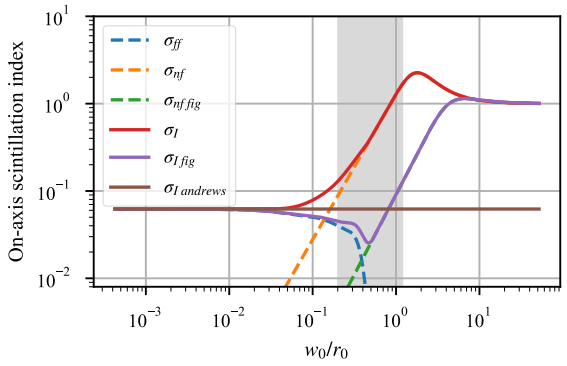

Figure A.3: Uplink scintillation index for Parenti and Andrews model, at $r_0 = 19cm$ and $\xi = 0\ deg$

Due to the need for beamwander modeling and implementation of tip-tilt adaptive optics correction on the uplink the discussion of scintillation probability density functions is restricted to that by Parenti. He suggests using separate probability density function for the near-field and far-field turbulence induced log-amplitude variance. With the near field turbulence being a log-normal distribution:

$$p_{NF}(S) = \frac{1}{S\sqrt{2\pi\left[\sigma_I^2\right]_{NF,\ fig}}} exp\left(\frac{-(ln(S) + \left[\sigma_I^2\right]_{NF,\ fig})^2}{2\left[\sigma_I^2\right]_{NF,\ fig}}\right) \tag{A.20}$$

and far field turbulence in a Weibull distribution:

$$p_{FF}(S) = \frac{\beta\,\Gamma(1+1/\beta)}{\langle S\rangle}\left[\Gamma(1+1/\beta)\frac{S}{\langle S\rangle}\right]^{\beta-1} exp\left(-\left[\Gamma(1+1/\beta)\frac{S}{\langle S\rangle}\right]^{\beta}\right), \tag{A.21}$$

with $\beta \approx [\sigma^2]_{NF}$. With the operating region under consideration in Figure A.3 visibly with varying contributions of near- and far-field effects we, following [29] combine these two pdf into one unified pdf:

$$p(S) = \frac{[\sigma_I^2]_{NF}^2}{[\sigma_I^2]_{FF}^2 + [\sigma_I^2]_{NF}^2} p_{NF}(S) + \frac{[\sigma_I^2]_{FF}^2}{[\sigma_I^2]_{FF}^2 + [\sigma_I^2]_{NF}^2} p_{FF}(S) \tag{A.22}$$

The combination of this modelling approach and pdf's has been validated by Parenti using 100,000 numerical simulations and are further corroborated by Andrews [30]. We have verified our implementation of this method by reproducing figures in [29] and [30], showing agreement with analytical and numerical results in both papers.

Downlink beam

Donwlink beam scintillation also follows from Andrews [10]. With the downlink beam notably approximated as a plane wave giving the Rytov variance as in Equation A.12 however with the third moment of turbulence μ_3 replaced with th first moment of turbulence μ_1, defined as:

$$\mu_1 = \int_{h_0}^{H} C_n^2(h) \left(\frac{h - h_0}{H - h_0} \right)^{5/6} dh \tag{A.23}$$

and the weak to strong turbulence adjusted scintillation index,

$$\sigma_I = exp \left[\frac{0.49\sigma_R^2}{\left(1 + 1.11\sigma_R^{12/5}\right)^{7/6}} + \frac{0.51\sigma_R^2}{\left(1 + 0.69\sigma_R^{12/5}\right)^{5/6}} \right] - 1 \tag{A.24}$$

with only a small adjustment in the denominator of the first term, indicating difference under moderate to strong fluctuations. With aperture size beyond that of the atmospheric coherence width the scintillation level measured by the receiving detector decreases by the aperture averaging factor.

$$A = \left[1 + 1.062 \frac{kD_g^2}{4L} \right]^{-7/6}, \ \sigma_R < 1 \tag{A.25}$$

Which can be implemented in Equation A.24 to account for aperture averaging [27],

$$\sigma_I = exp \left[\frac{0.49\sigma_R^2}{\left(1 + 0.18d^2 + 0.56\sigma_R^{12/5}\right)^{7/6}} + \frac{0.51\sigma_R^2 \left(1 + 0.69\sigma_R^{12/5}\right)^{-5/6}}{1 + 0.90d^2 + 0.62d^2\sigma_R^{12/5}} \right] - 1 \tag{A.26}$$

The aperture averaging effect is illustrated in Figure A.4 showing decreasing scintillation index for increasing receiving aperture area.

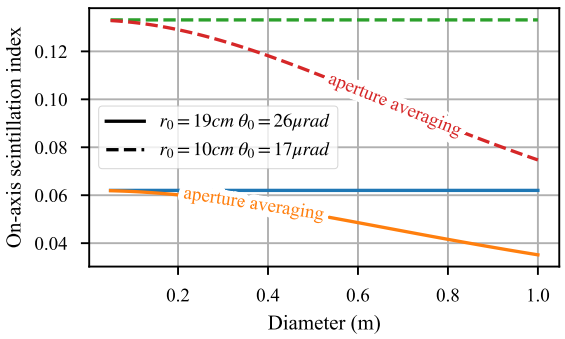

Figure A.4: Aperture averaging effect

To conclude the scintillation methodology, the significant impact of beamwander and the corresponding tip-tilt mitigation effect on uplink beams has been shown. Furthermore, downlink scintillation can be mitigated through aperture averaging, showing an approximate decrease in scintillation index of 0.5 for the conditions considered. Consequently we have chosen to implement both beamwander effects on the uplink and aperture averaging on the downlink for the optical link budget following the respective models defined here.

A.2.4. Anisoplanatism

One of the objectives of this study was to determine the link budget impact of anisoplanatism in tip-tilt corrected uplinks. Specifically, point ahead angle anisoplanatism which as a consequence of the orbital velocity of GEO and Tundra satellites creates an offset in the uplink and downlink path, illustrated in Figure A.5. At high altitudes the turbulence effects between the two beam are not correlated anymore, leading to less effective or even counter-productive tip-tilt correction. To estimate these effects various models have been investigated and implemented.

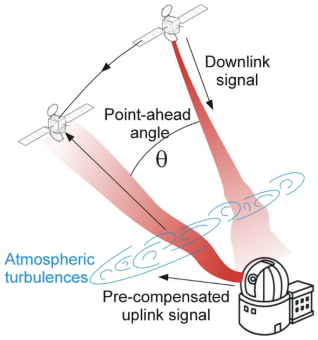

Figure A.5: Illustration of the point ahead angle [31]

It is important to distinguish anisoplanatism from anisokinetism. Where anisoplanatism refers to phase variance induced by variation of all Zernicke modes, anisokinetism is limited to only tip-tilt contributions. While anisokinetism accounts for the majority of anisoplanatism effect the aim is to ideally include the full anisoplanatism effect. It is possible in practice to mitigate anisoplanatism effects by the implementation of a laser guide, which can be used to sample Zernicke modes beyond tip-tilt leaving the remaining anisokinetism. This is however, left for future evaluations.

Sasiela method

From 'Electromagnetic wave propagation in turbulence' [23] turbulence induced phase variance has been extended to include anisoplanatic degradation of tip-tilt. The derivation given in chapter 3 will not be repeated here, instead a comparison and verification of this method is given.

Sasiela has also derived a 5-term approximation of the anisoplanatic degradation of the Strehl. To be used as a reference and defined as

$$SR = exp(-\sigma_\phi) \cdot (1 + 0.9736E + 0.5133E^2 + 0.2009E^3 + 0.06970E^4 + 0.02744E^5), \tag{A.27}$$

with

$$E_\theta = 6.88\mu_2/\mu_0 \cdot (\alpha_{paa}/d)^2 \cdot (d/r_0)^{5/3}, \tag{A.28}$$

and phase variance as

$$\sigma_\phi^2 = (\alpha_{paa}/\theta_0)^{5/3} \tag{A.29}$$

This approximation is notably only valid for small point ahead angles but provides a manor to verify the convergence of the Bessel function integral in the complete model. Which notably at small α_{paa} is not guaranteed to converge. In Figure A.6 this approximation is overlaid on the full model, showing excellent agreement until 8 μrad as expected from [23].

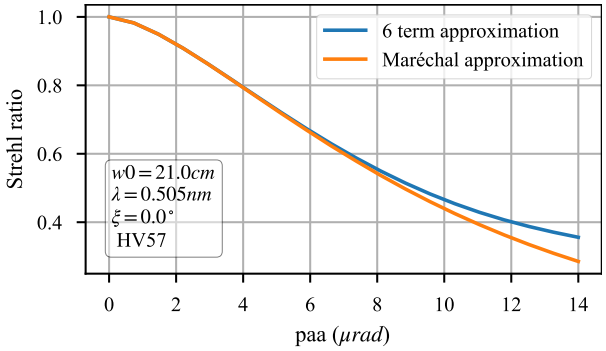

Figure A.6: Anisopanatism convergence verification Sasiel

The implementation of this anisoplanatism and anisokinetism has been further verified by reproducing double star simulation from Van Dam et al. [32]. An extensive research paper which furthermore provides the anisoplanatism and anisokinetism methodology with validation through double star measurements.

Alaluf/Valley method

As a comparison to the Sasiela method a different approach has been implemented as well. This is provided by Alaluf et al. [31] to estimate anisoplanatism losses to GEO as a mean jitter loss. This has been done following Valley, who determined an expression of tip-tilt angle decorrelation due to anisoplanatism [33].

$$\sigma_x^2 = 2[1 - C_{ax}(\theta)]\sigma_{tilt}^2 \tag{A.30}$$

$$\sigma_y^2 = 2[1 - C_{ay}(\theta)]\sigma_{tilt}^2 \tag{A.31}$$

With $\sigma_{tilt}^2 = 0.427\frac{\lambda}{D}\left(\frac{D}{r_0}\right)^{5/6}$ the atmospheric induced jitter [26] and C_{ax} and C_{ay} the respective correlation functions which can be written as [31],

$$C_{x,y}(\theta) = \frac{\int_0^{\text{inf}}[A_0(s) \mp A_2(s)]C_n^2(h)dh}{\int_0^{\text{inf}} C_n^2(h)dh} \tag{A.32}$$

with the following approximation (within 0.2% error):

$$\begin{aligned} A_0(s) &= exp(-0.5866s^{1.759}), 0 \leq s \leq 0.55 \\ &= 0.6656s^{-1/3}[1 + 1/(6^3s^2)], 0 < s \end{aligned} \tag{A.33}$$

$$\begin{aligned} A_2(s) &= exp(-1.941s^{-0.4602}), 0 \leq s \leq 0.625 \\ &= 0.1331s^{-1/3}[1 - 1/(6s^2)], 0.625 < s \end{aligned} \tag{A.34}$$

Where the two-axis rms anisokinetic jitter is then $\sigma_{TA}^2 = \frac{\sigma_x^2 + \sigma_y^2}{2}$. The losses of this tip-tilt error have been implemented as mean jitter loss,

$$L_{jitter} = e^{\left(\frac{-4\sigma_{TA}}{\theta_{div}}\right)^2} \tag{A.35}$$

A different approach to determine the mean losses then through the extended Maréchal approximation. Alaluf et al. further suggest using $1\sigma_{TA}$, $2\sigma_{TA}$ or $3\sigma_{TA}$ in Equation A.35 to determine a confidence interval. This inspired the approach chosen to expand the Sasiela methodology to include fade probability induced by anisokinetic jitter in addition to the mean Strehl loss, discussed in detail in chapter 3.

Transformation

Firstly, a transformation and comparison of two double-star validated methods is presented. From chapter 3 this can be done by converting the anisokinetic phase variance into a rms tip-tilt error [34],

$$\sigma_{TA}^2 = \sigma_\phi^2 \frac{2}{\pi^2} \left(\frac{\lambda}{D}\right)^2 \tag{A.36}$$

Alternatively, the tip tilt jitter can be seen as a reduction in diffraction limited resolution and subsequently in Strehl through [34]:

$$S \approx \left(\frac{[\lambda/D)^2 + (\sigma/0.42)^2]^{1/2}}{\lambda/D}\right)^{-2} \tag{A.37}$$

This transformation is shown in Figure A.7 with very good agreement of the methods just as in chapter 3.

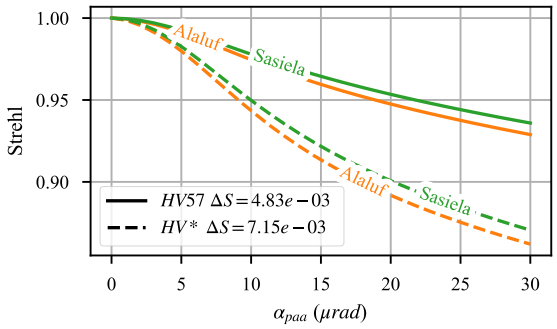

Figure A.7: Comparison mean tip-tilt anisokinetic loss, transformed to Strehl

A.2.5. Unified uplink scintillation distribution

While regular scintillation effects and that induced by anisoplanatism have been considered separately in this study, this would idealy be combined in one general distribution. The scintillation modelling method proposed by Shubert [35] could provide an opportunity to do so. Each mode is assumed independently Gaussian distributed, as has been done for the definition of anisokinetic fades. Here however, the distribution of higher order modes is included through the Xi-squared distribution.

Losses are evaluated through the Maréchal approximation using signal phase variance, being the sum of the variance induced by each individual mode. Given the assumption that each is Gaussian distributed the Strehl ratio can be expressed using a random variable χ_k^2 with κ degrees of freedom: $S = e^{-\Sigma\phi_n^2} = e^{-\frac{\phi}{k}\chi_k^2}$, with the probability then given by the chi-squared distribution [35],

$$p(S) = \frac{1}{2^{\kappa/2}\Gamma(\kappa/2)} \left[\frac{\kappa}{\sigma_\phi}\right]^{\kappa/2} - \ln(S)^{\kappa/2-1} S^{2/\sigma_\phi - 1} \tag{A.38}$$

for which Shubert has estimated the appropriate number of modes κ using Monte-Carlo wave optics simulation,

$$\kappa = \begin{cases} (D/r_0)^{-1/2} & , \ D/r_0 \leq 2 \\ (D/r_0 - 1.5)^{1/2} & , \ D/r_0 > 2 \end{cases} \tag{A.39}$$

Generating distributions for $0.5 < D/r_0 < 4$ we observe that using the phase variances as derived by Sasiela correspond very well to the Monte Carlo numerical wave propagation results generated by Shubert. This method allows us to estimate the cumulative density function of anisoplanatic losses, including higher order Zernicke modes beyond tip-tilt anisokinetism. This cumulative density function is given in Figure A.9. Similarly, the cdf for total scintillation, including anisoplanatism and regular scintillation effect is presented in Figure A.9.

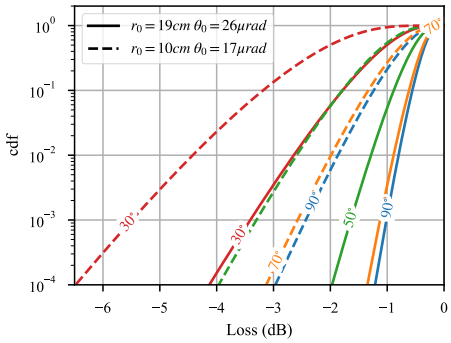

Figure A.8: Xi-squared distributed cdf of anisoplanatic scintillation $\alpha_{paa} = 18.5\mu rad\ D = 20cm$

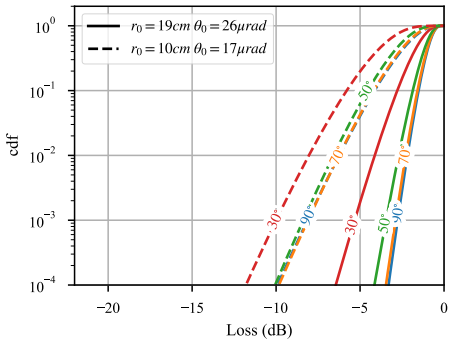

Figure A.9: Xi-squared distributed cdf of total scintillation $\alpha_{paa} = 18.5\mu rad\ D = 20cm$

While this approach offers the appealing prospect of unifying all sources of scintillation, including anisoplanatism, into a single model, the decision was made against its implementation. Upon reviewing the results and comparing them to the cumulative distribution function (CDF) generated for the previously established models (see Section chapter 3), the anticipated modest increase in anisoplanatism losses was observed due to the inclusion of higher-order modes. However, a significant limitation of this Xi-squared distribution approach in the current implementation becomes apparent as it fails to account for large-scale beam wander, resulting in a substantial reduction in the required scintillation margin. This is particularly problematic in the uplink regime where significant beam wander effects influence the scintillation index, as illustrated in Figure A.3. Therefore, while this methodology is intriguing for future research, it as been not considered further in this research.

B
Cloud-free-line-of-sight-probability

To support the analysis of link performance a preliminary analysis of availability conditions was performed. Taking cloud coverage data and projected availability figures from the proposed OGS network in Canada from Gagnon et al.[36]. The characteristics of the network are summarised in Table B.1.

Availability

Assuming uncorrelated cloud coverage for these groundstations the availability figure of the entire network can be computed as,

$$availability = \prod (1 - p_{cloud\ free}) \tag{B.1}$$

This availability figure has been adjusted to account for turbulence conditions exceeding the budgeted margin. Following the cumulative distribution function for r_0 and θ_0 in chapter 3 the mean HV57 and HV* condition were determined as 83% and 99% confidence interval conditions. Resulting respectively in a 0.83 and 0.99 probability that the budget turbulence condition is not exceeded. Adjusting the OGS network availability as:

$$availability = \prod (1 - p_{cloud\ free} \cdot p_{turbulence\ margin}) \tag{B.2}$$

Leading to a combined availability without account for turbulence of 92.16 %, for 99% confidence turbulence mitigation 91.92% and 83% confidence yields a 87.14% availability. Respectively, giving a 0.14 and 6.02 percent point loss of availability.

Note that this representation is a considerable simplification. As such r_0 and θ_0 are assumed uncorrelated, and the turbulence condition between sites as uncorrelated. This is not completely representative as turbulence conditions follow a diurnal pattern with notably a maximum on r_0 after noon and lulls around sunrise and sunset [37]. Furthermore, r_0 and θ_0 distributions have been generated.

Correlation analysis

To determine the validity of the uncorrelated availability analysis as presented in Gagnon et al., a cloud coverage analysis was performed. The NCEP North American Regional Reanalysis (NARR) dataset [38] has been used for this purpose, providing 8 times daily climatological data with 0.3 deg latitude and longitude accuracy. From this set the total cloud fraction dataset has been utilised, of which a single instance of the 2023 dataset has been presented in Figure B.1. The parameter cloud coverage fraction corresponds to the percentage of area within the dataset pixel which is has cloud coverage. This has

Table B.1: Potential Canadian OGS [36]

Location	Latitude (deg N)	Longitude (deg W)	Average Cloud Cover (%)
St. Hubert, QC	45.52	73.37	71.19
Edmonton, AB	53.68	113.48	71.99
Moose Jaw, SK	50.34	105.56	69.25
Gagetown, NB	45.84	66.44	72.10
Winnipeg, MB	49.90	97.23	70.35
Esquimalt, BC	48.44	123.43	71.44
Halifax, NS	44.66	63.59	76.28
Borden, ON	44.27	79.92	72.02

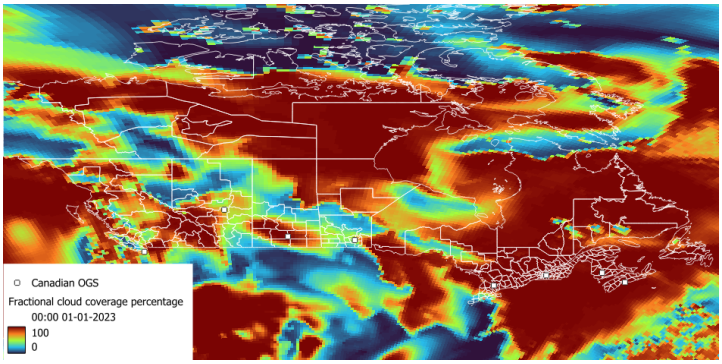

Figure B.1: Cloud coverage fraction over Canada

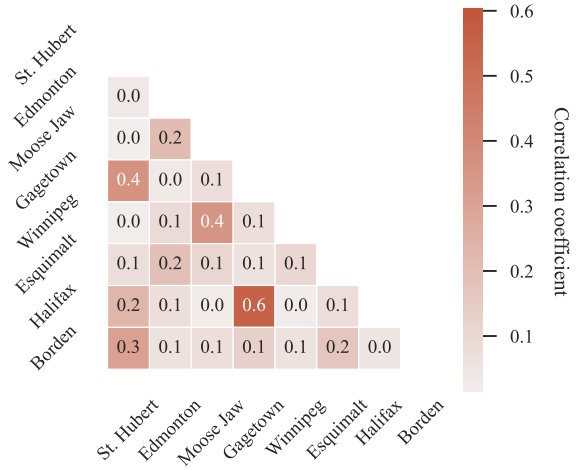

Figure B.2: Cloud coverage fraction correlation

been determined irrespective of cloud type, and thus does not consider possible cirrus cloud mitigation.

Comparing the correlation of the cloud coverage fraction presented in Figure B.2 no to weak correlation can be observed. However, the Eastern two OGS Gagetown and Halifax show quite strong positive correlation, as do most of the other eastern show moderate correlation. This brings into question the validity of the uncorrelated assumption in network availability results. While performing a new availability analysis incorporating correlation effects is out of scope the need for a detailed availability analysis for Canada is noted.

C
Orbit Coverage

Link geometry forms a central aspect in the Tundra orbit analysis for optical feederlinks. Necessitating the translation of orbit movements in inertial space to link viewing geometry for an OGS on Earth. Here the orbit generation, processing and transformation to link budget inputs will be discussed, notably how the coverage of two and three satellite constellations can be aggregated. Results pertaining to orbit coverage optimisation have been discussed in chapter 3.

C.1. Single satellite geometry

The satellite link geometry is firstly generated for a single orbit. This study has made use of the TU Delft Astrodynamics Toolbox (Tudat) to efficiently generate many Tundra orbits for analysis and optimisation purposes. Orbits have been propagated using idealised and closed form Keplerian equations of motions. Analysis of 3-body perturbations and gravity-field differentials effect on orbit stability and orbit control cost has been performed separate and is discussed in Appendix D.

Frame conversions

Orbits of interest are defined and propagated in Earth inertial space for 24 hours and stored, corresponding to the repeating ground track interval of Tundra orbits. The stored satellite state vectors are then transformed from Earth-centered Inertial space (ECI), specificaly J2000, to the co-rotating Earth-centered Earth-fixed space (ECEF). The position vector is rotated over the Earth rotating axis, the angle of which is defined by the Earth rotational speed ω_E and the time Δt since J2000 :

$$\begin{bmatrix} x \\ y \\ z \end{bmatrix}_{ECEF} = \begin{bmatrix} cos\ \omega_E \Delta t & sin\ \omega_E \Delta t & 0 \\ -sin\ \omega_E \Delta t & cos\ \omega_E \Delta t & 0 \\ 0 & 0 & 1 \end{bmatrix} \begin{bmatrix} x \\ y \\ z \end{bmatrix}_{ECI} \tag{C.1}$$

and ECEF velocity requiring the compensation of the rotational speed of the Earth.

$$\begin{bmatrix} \dot{x} \\ \dot{y} \\ \dot{z} \end{bmatrix}_{ECEF} = \begin{bmatrix} cos\ \omega_E \Delta t & sin\ \omega_E \Delta t & 0 \\ -sin\ \omega_E \Delta t & cos\ \omega_E \Delta t & 0 \\ 0 & 0 & 1 \end{bmatrix} \begin{bmatrix} \dot{x} \\ \dot{y} \\ \dot{z} \end{bmatrix}_{ECI} - \begin{bmatrix} 0 \\ 0 \\ \omega_E \end{bmatrix} \times \begin{bmatrix} x \\ y \\ z \end{bmatrix}_{ECEF} \tag{C.2}$$

The local coordinate frame of an observer is described in the East, North, Up coordinate frame (ENU), or local tangent plane coordinates on the spherical Earth. A last transformation which is made using the latitudinal λ and longitudinal ϕ position of the observer [39], given as

$$\begin{bmatrix} e \\ n \\ u \end{bmatrix}_{ENU} = \begin{bmatrix} -sin\ \lambda & cos\ \lambda & 0 \\ -cos\ \lambda\ sin\ \phi & -sin\ \lambda\ cos\ \phi & sin\ \phi \\ cos\ \lambda\ cos\ \phi & sin\ \lambda\ cos\ \phi & sin\ \lambda \end{bmatrix} \begin{bmatrix} x \\ y \\ z \end{bmatrix}_{ECEF} \tag{C.3}$$

with which the ENU unit vectors $\hat{\mathbf{e}}$, $\hat{\mathbf{n}}$, $\hat{\mathbf{u}}$ of the local observer/OGS coordinate frame can also be defined.

Pointing

By converting the satellite ephemeris to ECEF coordinates the relative position of the satellite to ground-station can be computed as $\mathbf{r}_{rel} = \mathbf{r}_{sat,\ ECEF} - \mathbf{r}_{OGS,\ ECEF}$. The elevation angle E and azimuth angle A can then computed as seen from the OGS:

$$E = arcsin(\hat{\mathbf{r}}_{rel} \cdot \hat{\mathbf{u}}_{OGS}), \tag{C.4}$$

$$A = arctan\left(\frac{\hat{\mathbf{r}}_{rel}\cdot\hat{\mathbf{e}}_{OGS}}{\hat{\mathbf{r}}_{rel}\cdot\hat{\mathbf{n}}_{OGS}}\right), \tag{C.5}$$

for which the link length is then simply the norm of $\mathbf{r}_{rel}$. The final satellite dependent link geometry parameter, the point ahead angle, can be determined decomposing the ECI velocity into

$$\dot{\mathbf{r}}_{tan} = \dot{\mathbf{r}}_{sat} - \frac{\mathbf{r}_{rel}\cdot\dot{\mathbf{r}}_{sat}}{||\mathbf{r}_{rel}||}\cdot\hat{\mathbf{r}}_{rel} \tag{C.6}$$

From which the point ahead angle is determined as $\alpha_{paa} = \frac{2||\dot{\mathbf{r}}_{tan}||}{c}$.

Verification & Validation strategy

Individual unit-testing has been performed on orbit generation and frame transformations by reproducing analysis performed in Systems Toolkit (STK). Elevation maps generated through the TUDAT implementation yielded the same results as verification through STK. Additionally, a complete integrated test of this routine has been performed to successfully reproduce link geometry and point-ahead angles for Sentinel-6 simulations and measurements by Lazzaro et al. [40]. Note that no propagation convergence or accuracy analysis had to be done for this approach following the description of the ephemeris using the closed form Keplerian equations of motion.

C.2. Constellation geometry

The configuration of the constellations of two and three Tundra satellite can be defined as a Flower constellation, with non-zero eccentricity and repeating geometry. While such constellation are highly complex to analyse these restrictions to Tundra with 24h repeating ground tracks greatly simplified the analysis. In addition the following characteristics are defined:

- Orbits have the same in-plane shape. Thus same eccentricity, inclination and semi-major axis.
- Satellites are distributed in different planes with equal spacing. For two satellites thus $\triangle$LAN 180 deg and for three satellites 120 deg.
- Satellite mean-anomaly are distributed with equal spacing. For two satellites thus by a mean anomaly offset of 1/2 and three satellite by 1/3.
- Apogee latitude is positioned at point of highest latitude. Giving argument of perigee of 270 deg for all orbits.

The above restrictions define a Tundra constellation which has an identical groundtrack for all satellites and even phasing of satellite apogee passes over 24h, providing the ideal coverage scenario. While varying in-plane orbit shapes could provide orbit control benefits, as shown by Bruno and Pernicka [8], coverage consistency is deemed more relevant for a study involving link geometry subtleties. Furthermore, the definition of one satellite would define that of the rest of the constellation following restriction two and three, simplifying analysis.

The link geometry of all satellites in a constellation is subsequently computed over the region or points of interest. The combined coverage of two or three satellites is determined by merging and selecting the satellite with the highest elevation angle for each epoch over the 24h propagation, as illustrated in Figure C.2.

Handovers and active satellites

This approach of combining satellite coverage by down-selecting to the highest elevation satellite is specific to this analysis, where generally the % of time with coverage or number of satellites in view would be of interest. Owing to the repeating elevation profile for regions under the Tundra orbit apogee, the satellite exhibits a predictable rise and fall in elevation with the payload active around the apogee. Optical feeder links are highly directive and would only be connected to one of the two satellites in view at the time. The distinction of highest elevation is an effective manner to switch from the falling to rising satellite, this approach is illustrated in Figure C.1. Due to differences in relative link geometry these optimum hand-over point would occur at different moments in time for different OGS location.

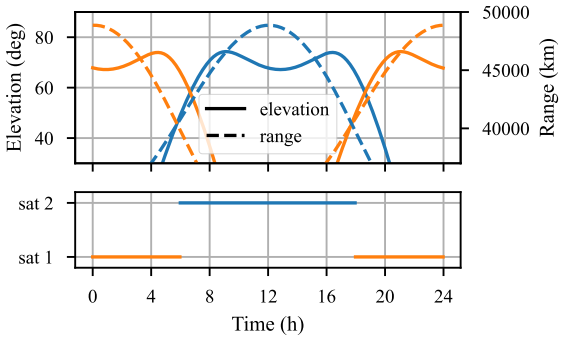

Figure C.1: Link handover for max elevation

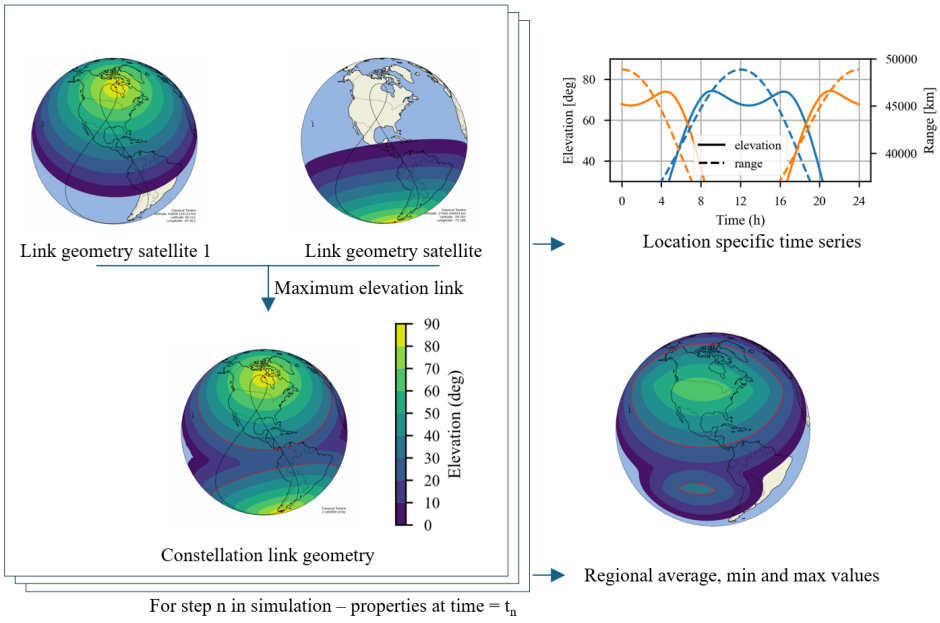

Figure C.2: Caption

An alternative approach considering a link choice for the link geometry corresponding to the smallest path losses was also implemented. Notable in this approach is that under favorable atmospheric conditions, and for high eccentricity (0.3+) orbits in a three satellite constellation, the highest elevation link would not be the most favourable link from path loss perspective. Following from moderate atmospheric losses with respect to the large free-space losses at satellite apogee. This would result in additional link switches from the satellite at apogee to a rising satellite. However this, 'optimal' approach, would incur unwanted additional link handovers. Consequently the highest link elevation approach was maintained, providing an optimal implementable solution.

From the previous definition of Tundra constellations the combined link geometry is analysed as time series for link geometry to specific geographical locations or as a time-average/min/max over larger regions, as illustrated in Figure C.2. The former are implemented for detailed link computations while the latter has been used for constellation option comparisons and trade-offs.

D
Orbit Control Costs

To asses implementation feasibility and identify trade-off driving characteristics of Tundra orbits an evaluation of ΔV cost pertaining to orbit control, insertion and end-of-life has been performed. This appendix will cover the computation of orbit control cost given a set of perturbed orbital elements. It is important to note that the following analysis is performed for impulsive ΔV manoeuvres, and that the applicability of these results to low-impulse propulsion is limited.

With long-term numerical propagation out of scope, the orbit control costs result from general orbital element variations for Tundra orbits generated by Fantino et al. [41]. In which 2-year numerical propagation has been performed for a set of Tundra orbits with eccentricity varying from 0.25 to 0.4, inclination varying from 55 to 70 deg, spaced over 60 deg RAAN increments. The variations of the orbital elements provides a general case for wich budgeting can be performed, as due to relative RAAN positioning of a satellite to the Sun and Moon will cause varied orbital evolution within a constellation.

Bruno and Pernicka [8] derived from the Merovitch expressions of orbital elements perturbations due to tangential and normal perturbations. Formulations which can be used here to provide the required ΔV impulses for the adjustment of the orbital elements.

The maintenance of various orbital elements can be combined into one of two type of manoeuvres: normal out-of-plane manoeuvre or transverse in-plane manoeuvres. Generally speaking out-of-plane manoeuvres consisting of inclination and RAAN change are the most costly. Consequently, in chapter 3 different station keeping strategies are discussed to minimise the need for such out-of-plane control. Here however, the discussion will include all element control, from which free perturbing elements can simply be omitted in the computation.

Normal manoeuvre

Firstly considering the normal manoeuvre which can be used to control inclination i, RAAN Ω and the argument of perigee ω. Note that the argument of perigee is altered by the normal and transverse manoeuvre, of which the latter is much more efficient. Consequently the change in argument of perigee by the normal burn is considered as an additional perturbation to be corrected in the transverse burn. The true anomaly at which the normal manoeuvre is performed will impact its effectiveness due to the non-zero orbit eccentricity and should optimised to combine RAAN and inclination burn by

$$v_n = arctan\left(\frac{\Delta\Omega sin\ i}{\Delta i}\right) - \omega, \tag{D.1}$$

with the radius r at true anomaly v and mean motion n as,

$$r = \frac{a(1-e^2)}{1 + e\ cos\ v}, \tag{D.2}$$

$$n = \sqrt{\frac{\mu}{a^3}} \tag{D.3}$$

The combined normal burn for inclination and RAAN correction can then be computed as a single normal burn,

$$\Delta V_n = \Delta i \frac{na^2\sqrt{1-e^2}}{r\ cos(\omega + v)}, \tag{D.4}$$

or alternatively via

$$\Delta V_n = \Delta\Omega \frac{na^2\sqrt{1-e^2} sin\ i}{r\ sin(\omega + v)}. \tag{D.5}$$

From the Merovitch expression of orbital elements the argument of perigee variation induced by the normal burn then is,

$$\Delta\omega = -\Delta V_n \frac{\sqrt{1-e^2}}{nae} \frac{re\ cot\ i\ sin(\omega + v)}{a(1-e^2)} \tag{D.6}$$

Transverse manoeuvre

In the transverse manoeuvre some simplifications are applied to the method by Bruno and Pernick. A normal burn ought to split into two burn components correct for semi-major axis, eccentricity and argument of perigee. As performing the burn at the correct true-anomaly for two parameters would offset the third. However, following the very small semi-major axis contribution for stationkeeping costs [41] this aspect is not taken into account by ignoring semi-major axis effects, consequently:

$$\Delta V_t = \Delta a \frac{nr}{2a\sqrt{1-e^2}} \approx 0 \tag{D.7}$$

The resulting manoeuvre would then be performed at perigee as the most effective location,

$$\Delta V_t = \Delta e \frac{ner}{\sqrt{1-e^2}(1-e^2-r^2/a^2)} \tag{D.8}$$

The perigee manoeuvre can thus be simplified to:

$$\Delta V_t = \Delta\omega \frac{nae}{\sqrt{1-e^2}[1+r/a(1-e^2)]sin\ v} = \Delta\omega \frac{e}{2\sqrt{\mu/[a(1-e^2)]}} \tag{D.9}$$

Effectiveness

Evident from the above expression is that eccentricity and inclination will affect the cost associated to stationkeeping. Of particular interest is the effect of higher eccentricity, which results in an increased cost of perigee rotation correction as illustrated in Figure D.1. This phenomenon is significant, and has thus been accounted for in the analysis when considering the effects of the Earth's J2 oblateness in orbit selection. Variations of the other element corrections has not been considered in detail in orbit trade-off, this would however be of interest for future detailed orbit stationkeeping analysis combined with numerical orbit propagation.

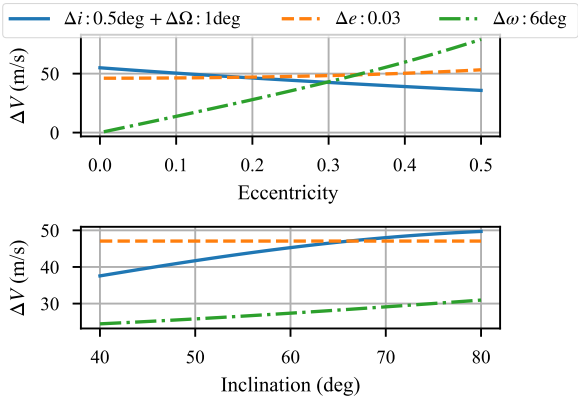

Figure D.1: Stationkeeping manoeuvre ΔV costs varying for eccentricity (i:63.4) and inclination (e:0.2658)

References

[1] Development Sector. *Facts and Figure*. Tech. rep. ITU, 2022.

[2] Euroconsult. *Non-geostationary orbit constellations redefining the High Throughput Satellites market landscape*. April 25, 2024 https://www.euroconsult-ec.com/press-release/non-geostationary-orbit-constellations-redefining-the-high-throughput-satellites-market-landscape/. (Accessed: 13 May 2024).

[3] Riccardo De Gaudenzi et al. "Future technologies for very high throughput satellite systems". In: *International Journal Satellite Communications Networking* 38 (2020), pp. 141–161.

[4] Amar Mody and Eva Gonzalez. "An operator's view: The medium-term feasibility of an optical feeder link for VHTS". In: *2017 IEEE International Conference on Space Optical Systems and Applications (ICSOS)*. IEEE. 2017, pp. 278–285.

[5] Ramon Mata Calvo et al. "Optical feeder links for very high throughput satellites-system perspectives". In: (2015).

[6] Harald Hauschildt et al. "European data relay system goes global". In: *2017 IEEE International Conference on Space Optical Systems and Applications (ICSOS)*. 2017, pp. 15–18. DOI: 10.1109/ICSOS.2017.8357204.

[7] Alan Kidd and Ali Shoamanesh. "System Tradeoffs for the Global Radio Space Segment". In: *20th AIAA International Communication Satellite Systems Conference and Exhibit*. 2002, p. 2040.

[8] Michael J Bruno and Henry J Pernicka. "Tundra constellation design and stationkeeping". In: *Journal of spacecraft and rockets* 42.5 (2005), pp. 902–912.

[9] Dirk Giggenbach and Amita Shrestha. "Atmospheric absorption and scattering impact on optical satellite-ground links". In: *International Journal of Satellite Communications and Networking* 40.2 (2022), pp. 157–176.

[10] Larry C Andrews, Ronald L Phillips, and Cynthia Y Young. "Scintillation model for a satellite communication link at large zenith angles". In: *Optical Engineering* 39.12 (2000), pp. 3272–3280.

[11] Nicolas Védrenne et al. "First experimental demonstration of adaptive optics pre-compensation for GEO feeder links in a relevant environment". In: *2019 IEEE International Conference on Space Optical Systems and Applications (ICSOS)*. IEEE. 2019, pp. 1–5.

[12] Bischl H. et al. *Feasibility Assessment of Optical Technologies and Techniques for Reliable High Capacity Feeder Links*. Tech. rep. ESA, 2010.

[13] Larisa D Trichtchenko et al. "Highly elliptical orbits for arctic observations: Assessment of ionizing radiation". In: *Advances in Space Research* 54.11 (2014), pp. 2398–2414.

[14] Marko Höyhtyä et al. "Sustainable satellite communications in the 6G era: A European view for multi-layer systems and space safety". In: *IEEE Access* (2022).

[15] John Draim and David Castiel. "Elliptic constellations for optimal coverage of selected geographical areas". In: *16th International Communications Satellite Systems Conference*. 1996, p. 1075.

[16] Yuri Ulybyshev. "Satellite constellation design for continuous coverage: short historical survey, current status and new solutions". In: *Proceedings of Moscow Aviation Institute* 13.34 (2009), pp. 1–25.

[17] Sylvain Poulenard, Michael Crosnier, and Angélique Rissons. "Ground Segment Design for Broadband Geostationary Satellite With Optical Feeder Link". In: *Journal of Optical Communications and Networking* 7.4 (2015), pp. 325–335.

[18] Hemani Kaushal, V.K. Jain, and Subrat Kar. *Free Space Optical Communication*. Springer, 2017. ISBN: 1935-3839.

[19] Bernard Roy et al. “Optical feeder links for high throughput satellites”. In: *2015 IEEE International Conference on Space Optical Systems and Applications (ICSOS)*. IEEE. 2015, pp. 1–6.

[20] F. Kneizys et al. “User guide to LOWTRAN 7”. In: (Aug. 1988), p. 146.

[21] Meg Noah. *LOWTRAN7 Aerosol Models and Atmosphere Profile Data*. MATLAB Central File Exchange, 22 April 2019 https://www.mathworks.com/matlabcentral/fileexchange/71018-lowtran7-aerosol-models-and-atmosphere-profile-data. Accessed: 12 April 2024.

[22] Michael Hirsch. *lowtran 3.1.0*. Pypi, February 2023 https://pypi.org/project/lowtran/3.1.0/. Accessed: 12 April 2024.

[23] Richard J Sasiela. *Electromagnetic wave propagation in turbulence: evaluation and application of Mellin transforms*. Vol. 18. Springer Science & Business Media, 2012.

[24] Larry C Andrews and Ronald L Phillips. “Laser beam propagation through random media”. In: *Laser Beam Propagation Through Random Media: Second Edition* (2005).

[25] Meinhard T. Schobeiri. “Turbulent Flow, Modeling”. In: *Tensor Analysis for Engineers and Physicists - With Application to Continuum Mechanics, Turbulence, and Einstein’s Special and General Theory of Relativity*. Cham: Springer International Publishing, 2021, pp. 163–204. ISBN: 978-3-030-35736-8. DOI: 10.1007/978-3-030-35736-8_9. URL: https://doi.org/10.1007/978-3-030-35736-8_9.

[26] Robert J Noll. “Zernike polynomials and atmospheric turbulence”. In: *JOsA* 66.3 (1976), pp. 207–211.

[27] Larry C Andrews, Ronald L Phillips, and Cynthia Y Hopen. *Laser beam scintillation with applications*. Vol. 99. SPIE press, 2001.

[28] Larry C Andrews et al. “Beam wander effects on the scintillation index of a focused beam”. In: *Atmospheric Propagation II*. Vol. 5793. SPIE. 2005, pp. 28–37.

[29] Ronald Parenti et al. “Modeling the PDF for the irradiance of an uplink beam in the presence of beam wander”. In: *Atmospheric Propagation III*. Vol. 6215. SPIE. 2006, pp. 42–54.

[30] Larry C Andrews et al. “PDF models for uplink to space in the presence of beam wander”. In: *Atmospheric Propagation IV*. Vol. 6551. SPIE. 2007, pp. 92–103.

[31] D Alaluf and JM Perdigues Armengol. “Ground-to-satellite optical links: how effective is an uplink Tip/Tilt pre-compensation based on the satellite signal?” In: *CEAS Space Journal* (2021), pp. 1–12.

[32] Marcos A van Dam et al. “Angular anisoplanatism in laser guide star adaptive optics”. In: *Advances in Adaptive Optics II*. Vol. 6272. SPIE. 2006, pp. 987–995.

[33] George C Valley. “Isoplanatic degradation of tilt correction and short-term imaging systems”. In: *Applied Optics* 19.4 (1980), pp. 574–577.

[34] Scot S Olivier and Donald T Gavel. “Tip–tilt compensation for astronomical imaging”. In: *JOSA A* 11.1 (1994), pp. 368–378.

[35] Paul D Shubert. “Atmospheric fade probability in moderate aperture laser communication systems”. In: *Free-Space Laser Communications XXXI*. Vol. 10910. SPIE. 2019, pp. 340–347.

[36] Stephane Gagnon et al. “Recent developments in satellite laser communications: Canadian context”. In: *Proceedings of 2012 International Conference on Space Optical Systems and Applications*. 2012, pp. 9–12.

[37] DL Walters, DL Favier, and JR Hines. “Vertical path atmospheric MTF measurements”. In: *JOSA* 69.6 (1979), pp. 828–837.

[38] Fedor Mesinger et al. “North American regional reanalysis”. In: *Bulletin of the American Meteorological Society* 87.3 (2006), pp. 343–360.

[39] J. Sanz Subirana, J.M. Juan Zornoza, and M. Hernández-Pajares. *Transformations between ECEF and ENU coordinates*. ESA nauipedia, 2011 https://gssc.esa.int/navipedia/index.php/Transformations_between_ECEF_and_ENU_coordinates. (Accessed: 12 March 2024).

[40] Riccardo Lazzaro and Carlo Bettanini. “Evaluation of Satellite’s Point-Ahead Angle Derived from TLE for Laser Communication”. In: *Aerotecnica Missili & Spazio* 101.1 (2022), pp. 7–15.

[41] Elena Fantino et al. “Geosynchronous inclined orbits for high-latitude communications”. In: *Acta Astronautica* 140 (2017), pp. 570–582.